

# Molecular resonance and highly deformed fission fragments in $^{28}\text{Si}+^{28}\text{Si}$

C. Beck,\* R. Nouicer,† D. Disdier,‡ G. Duchêne, G. de France,§ R. M. Freeman, F. Haas, A. Hachem,||  
D. Mahboub,¶ V. Rauch, and M. Rousseau

*Institut de Recherches Subatomiques, UMR7500, Institut National de Physique Nucléaire et de Physique des Particules—Centre National de la Recherche Scientifique/Université Louis Pasteur, 23 rue du Loess, B.P. 28, F-67037 Strasbourg Cedex 2, France*

S. J. Sanders

*Department of Physics and Astronomy, University of Kansas, Lawrence, Kansas 66045*

A. Szanto de Toledo

*Departamento de Física Nuclear, University of São Paulo, Brazil*

(Received 5 September 2000; published 19 December 2000)

A high-resolution measurement of fragment-fragment- $\gamma$  triple coincidence events in the symmetric and near-symmetric mass exit channels from the  $^{28}\text{Si}+^{28}\text{Si}$  reaction has been undertaken using the EUROGAM Phase II  $\gamma$ -ray spectrometer. The bombarding energy of  $E_{\text{lab}}(^{28}\text{Si}) = 111.6$  MeV has been selected to populate the conjectured  $J^\pi = 38^+$  quasimolecular resonance in the  $^{56}\text{Ni}$  dinuclear system. In the  $^{28}\text{Si}+^{28}\text{Si}$  symmetric mass exit channel, the resonance behavior is clearly verified at the chosen energy. The population of highly excited states in the  $^{24}\text{Mg}$ ,  $^{28}\text{Si}$ , and  $^{32}\text{S}$  nuclei is discussed within a statistical fusion-fission model. Evidence is presented for selective population of states in the  $^{28}\text{Si}$  fragments arising from the symmetric fission of the  $^{56}\text{Ni}$  compound nucleus. The enhanced population of the  $K^\pi = 3_1^-$  band of the  $^{28}\text{Si}$  nucleus, indicative of an oblate deformed shape, suggests that the oblate configuration plays a significant role in the resonant process. Fragment angular distributions for the elastic and low-lying inelastic channels as well as  $\gamma$ -ray angular correlations for the mutual inelastic channel ( $2^+, 2^+$ ) indicate that the spin orientations of the outgoing fragments are perpendicular to the orbital angular momentum. This unexpected result, which is different from the alignment found for the resonance structures in the  $^{24}\text{Mg}+^{24}\text{Mg}$  and  $^{12}\text{C}+^{12}\text{C}$  systems, suggests a situation where two oblate  $^{28}\text{Si}$  nuclei interact in an equator-to-equator stable molecular configuration. A discussion concerning the spin alignment and spin disalignment for different reactions such as  $^{12}\text{C}+^{12}\text{C}$ ,  $^{24}\text{Mg}+^{24}\text{Mg}$ , and  $^{28}\text{Si}+^{28}\text{Si}$  is presented.

DOI: 10.1103/PhysRevC.63.014607

PACS number(s): 25.70.Ef, 25.70.Jj, 23.20.En, 27.40.+z

## I. INTRODUCTION

In heavy-ion physics the search for extremely deformed states in light-mass nuclear systems ( $20 \leq A_{\text{CN}} \leq 40$ ) has a long history [1–3] dating back to the early 1960's and the pioneering discovery of nuclear molecules in the  $^{12}\text{C}+^{12}\text{C}$  composite system studied at energies in the vicinity of the Coulomb barrier [4]. Correlated gross and intermediate-width resonant structures in the excitation functions at energies well above the Coulomb barrier were subsequently discovered in  $^{12}\text{C}+^{12}\text{C}$  reactions [1,5] as well as in reaction with other  $\alpha$ -like systems such as  $^{12}\text{C}+^{16}\text{O}$  and  $^{16}\text{O}+^{16}\text{O}$  [2,3]. In some systems very narrow width (barrier top) resonances were found to coexist with broad (potential) resonances, suggesting different physical processes [2,5]. The

study of molecular resonances evolved later with the unexpected observation of pronounced, narrow and well isolated resonances in various elastic and inelastic excitation functions measured for medium-mass nuclear systems ( $40 \leq A_{\text{CN}} \leq 60$ ) [6], also at energies well above the Coulomb barrier. The first observation of such high-spin resonances in this mass range was reported by Betts *et al.* [7–12] in the elastic and inelastic  $^{28}\text{Si}+^{28}\text{Si}$  scattering. Even more pronounced resonant structures were reported thereafter in the neighboring  $^{24}\text{Mg}+^{24}\text{Mg}$  system [13–17]. Resonance structures were also found in the asymmetric  $^{24}\text{Mg}+^{28}\text{Si}$  system [18,19]. However, the occurrence of such resonant structures is by no means universal, as other studies have revealed that several other nearby  $\alpha$ -particle systems lack similar structures. For instance, symmetric systems such as  $^{32}\text{S}+^{32}\text{S}$  [20] and  $^{40}\text{Ca}+^{40}\text{Ca}$  [11] exhibit structureless excitation functions, and the non- $\alpha$ -particle systems of  $^{28}\text{Si}+^{30}\text{Si}$  and  $^{30}\text{Si}+^{30}\text{Si}$  show no hint of resonant behavior [6]. At the time, the moleculelike sequences of resonances observed in  $^{24}\text{Mg}+^{24}\text{Mg}$  and  $^{28}\text{Si}+^{28}\text{Si}$  with measured angular momenta up to  $L = 42\hbar$  represented some nuclear excitations with the highest spins ever observed. The number of open channels model [21] (NOC) has been highly successful in selecting the systems showing resonance behavior. In this model [21], the main condition for observing a resonance behavior is associated with surface transparency. Particularly

\*Corresponding author. Electronic address: christian.beck@ires.in2p3.fr

†Present address: University of Illinois at Chicago, Chicago, IL and Brookhaven National Laboratory, Upton, NY.

‡Deceased.

§Permanent address: GANIL, Caen, France.

||Permanent address: Université de Nice-Sophia-Antipolis, Nice, France.

¶Present address: University of Surrey, Guildford, UK.

favorable cases are the  $^{24}\text{Mg}+^{24}\text{Mg}$  and  $^{28}\text{Si}+^{28}\text{Si}$  reactions [22], where the corresponding optical model (OM) potentials have small imaginary components at distances corresponding to peripheral collisions. In this paper we will discuss more fully the latter reaction which populates the  $^{56}\text{Ni}$  composite system.

For the  $^{28}\text{Si}+^{28}\text{Si}$  system [10–12], the intermediate-width structures [9] (with very narrow widths of  $\approx 150$  keV), superimposed on series of broad, fragmented structures [7,8] (with width of  $\approx 1$ – $2$  MeV), have been observed to be strongly correlated in angle, for at least five different exit channels [elastic scattering, single  $2_1^+$  excitation, mutual ( $2_1^+, 2_1^+$ ) and ( $2_1^+, 4_1^+$ ) excitations as well as excitations of higher states of the outgoing  $^{28}\text{Si}$  nuclei]. These narrow structures were clearly shown to be incompatible with statistical Ericson fluctuations [12], and most likely correspond to quasimolecular states in the compound nucleus (CN)  $^{56}\text{Ni}$  at high excitation energy ( $E_{\text{CN}}^* = 60$ – $75$  MeV) and high angular momenta ( $L = 34$ – $42\hbar$ ). These high values of angular momenta are of special interest since they approach the limit ( $L_{\text{limit}} = 45\hbar$ ) where, according to the rotating liquid drop model [23], the compound system  $^{56}\text{Ni}$  should disintegrate spontaneously under the stress of the centrifugal forces because of a vanishing fission barrier.

The total back-angle inelastic  $^{28}\text{Si}+^{28}\text{Si}$  scattering yield (with a total averaged cross section of  $\approx 1$  mb/sr measured at the energy of the  $38^+$  resonance [12]) has been found to be quite large and to have many of the characteristics of complete damping of energy and angular momentum similar to those expected for fusion-fission (FF) of the excited  $^{56}\text{Ni}$  CN [24]. The opening of the fission channel and the degree in which it affects elastic scattering and other binary channels were examined for the  $^{16}\text{O}+^{40}\text{Ca}$  [25–27] and the  $^{32}\text{S}+^{24}\text{Mg}$  [28–32] entrance channels, both populating the  $^{56}\text{Ni}$  CN. In recent years, extensive efforts have been devoted to the study of the FF dynamics of very light dinuclear systems ( $40 \leq A_{\text{CN}} \leq 60$ ) [24,33,34]. Statistical decay processes [24,35] have been demonstrated to influence reaction channels that have been previously explored in terms of heavy-ion resonance mechanisms (as is the case for the  $^{48}\text{Cr}$  CN [36]). The FF mechanism is known to play a significant role at spins slightly below the grazing angular momentum; the nuclear configuration leading to the resonance behavior is only slightly more elongated than that of the nuclear saddle point [33]. It has already been shown [31,35] that the statistical fission of the  $^{56}\text{Ni}$  CN and the molecular resonances arising from very deformed configurations of this composite system can occur in the same reaction channels.

It is conceivable that a coherent framework exists which connects the topics of heavy-ion molecular resonances, superdeformation, hyperdeformation, and fission shape isomerism [6,26,37–41]. In particular, shell-stabilized, highly deformed configurations [as illustrated by the existence of hyperdeformed second minima in potential energy surfaces (PES) calculated using the Nilsson-Strutinsky model] in  $^{56}\text{Ni}$  have been conjectured [6] to explain the strong resonant behavior observed at large angles for the  $^{28}\text{Si}+^{28}\text{Si}$  reaction [8]. Bengtsson *et al.* [37,38] have studied the shell correc-

tions for  $J=40$  and find evidence for a PES minimum corresponding to a hyperdeformed, prolate nuclear shape with a 3:1 major-to-minor axis ratio. The very striking molecular resonant structure of  $^{28}\text{Si}+^{28}\text{Si}$  was suggested to be possibly correlated to a rather special subset of high-spin states built upon this hyperdeformed minimum and stabilized against mixing into the more numerous CN states by some special symmetry [6]. These secondary minima can give rise to quasisustainable, shape-isomeric states. In the energy range corresponding to the  $J^\pi = 38^+$  resonance, the excitation energy of the CN is approximately  $E_{\text{CN}}^* = 65$  MeV and the density of  $J=38$  states can be estimated to be of several thousands of levels per MeV. Hence, the overlap of resonant wave functions with the normal CN states may be small, inhibiting the mixing between the two types of states and enhancing the lifetime of the isomer. The hyperdeformed states would be populated by all entrance channels that lead to the  $^{56}\text{Ni}$  CN formation, with strengths proportional to the decay width of the shape isomer in the entrance channel. An indication of these features has been given by Dichter *et al.* [26] who found that the intermediate-width structures are correlated in both the  $^{28}\text{Si}+^{28}\text{Si}$  and  $^{16}\text{O}+^{40}\text{Ca}$  systems. The strong correlation suggests that the resonances proceed through the  $^{56}\text{Ni}$  CN and that they may be the manifestations of shape isomeric superdeformed or hyperdeformed states in secondary minima in the PES. However, the PES calculations [37,38] are still far too schematic to enable any detailed comparison with the data. For example, based on a molecular model [42–46], a stable configuration of the  $^{28}\text{Si}+^{28}\text{Si}$  dinuclear system is found to arise from oblate deformed  $^{28}\text{Si}$  nuclei in their equator-to-equator configuration, due to the oblate deformed shape of the  $^{28}\text{Si}$  nuclei [44]. This contrasts with the prolate configuration suggested by Bengtsson [37,38]. We have proposed that the vanishing spin alignment in  $^{28}\text{Si}+^{28}\text{Si}$  may be considered as one of the first experimental indications of such a triaxial nuclear molecule [47]. More recently an alternate theoretical approach has been advanced which favors a description in terms of hyperdeformed quasimolecules formed in the  $^{28}\text{Si}+^{28}\text{Si}$  scattering process [48].

In this paper, we present the results of particle- $\gamma$  coincidence measurements for the  $^{28}\text{Si}+^{28}\text{Si}$  system. The paper focuses on how the fission yield is distributed among the possible mutual excitations of the fragments in the symmetric and near-symmetric mass channels. The coexistence of fission and a separate reaction mechanism corresponding to molecular resonances will be emphasized.

The paper is organized as follows. After a description of the experimental techniques in Sec. II, the experimental data of the fragment-fragment coincidence events and for the fragment-fragment- $\gamma$  coincidence events are presented in Secs. III and IV, respectively. Section V contains an overall discussion of the present  $^{28}\text{Si}+^{28}\text{Si}$  experimental data which are compared first with similar results obtained for both the  $^{12}\text{C}+^{12}\text{C}$  and the  $^{24}\text{Mg}+^{24}\text{Mg}$  systems, and secondly with recent theoretical studies of  $^{28}\text{Si}+^{28}\text{Si}$  scattering. The paper concludes with a brief summary given in Sec. VI.

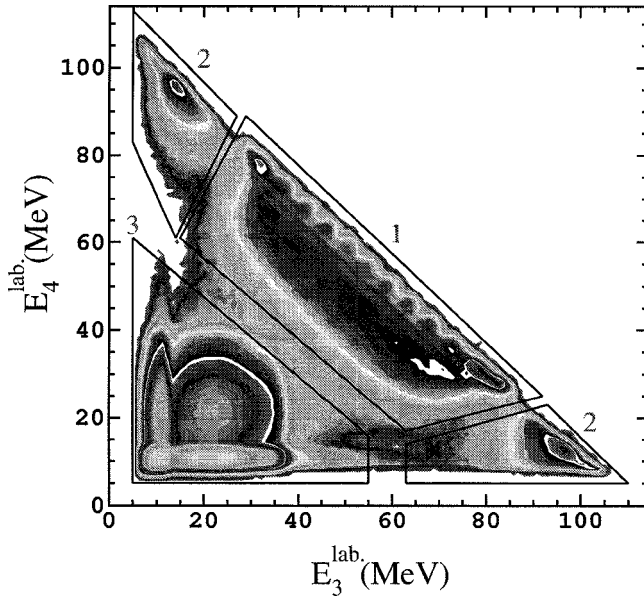


FIG. 1. Two-dimensional energy spectrum  $E_4$  versus  $E_3$  of the fragments detected by one pair of position-sensitive detectors for the  $^{28}\text{Si}+^{28}\text{Si}$  reaction at  $E_{\text{lab}}=111.6$  MeV. The regions labeled 1, 2, and 3 are explained in the text.

## II. EXPERIMENTAL PROCEDURES AND DATA ANALYSIS

The experiment was performed at the VIVITRON Tandem accelerator of the IReS in Strasbourg using the EURO-GAM phase II multidetector array [49]. The bombarding energy  $E_{\text{lab}}(^{28}\text{Si})=111.6$  MeV was carefully chosen [47] so as to populate the  $J=38^+$  resonance [6,8,9] of this system. The beam struck a  $25 \mu\text{g}/\text{cm}^2$  thick  $^{\text{nat}}\text{Si}$  (92% of  $^{28}\text{Si}$ ) target. The Si target thickness corresponds to a beam energy loss of  $\Delta E=130$  keV, which is smaller than the width of the resonance ( $\Gamma_{\text{lab}}\approx 300$  keV). Additional targets of Au ( $14 \mu\text{g}/\text{cm}^2$  thick) with a  $^{12}\text{C}$  ( $10 \mu\text{g}/\text{cm}^2$  thick) backing were used for calibration, background determination, and normalization purposes. Two pairs of large-area position-sensitive Si (surface-barrier) detectors (PSD) were used to detect the fission fragments in coincidence using standard techniques [50,51]. One pair was located in the horizontal plane at azimuthal angles of  $0^\circ$  and  $180^\circ$ , and the other in the vertical plane at azimuthal angles of  $90^\circ$  and  $270^\circ$ . Typical two-dimensional energy spectra are given in Figs. 1 and 2, and typical excitation-energy spectra are displayed in Figs. 3 and 4. The PSD's covered the laboratory angular range  $22^\circ$  to  $73^\circ$  in both the horizontal and vertical planes with solid angles of  $114$  msr, and an azimuthal angular acceptance of  $\pm 4^\circ$ . The mass identification of the two binary fragments, displayed in Fig. 5, was done using standard two-body kinematics formulas [52,53] leading to a mass resolution  $\Delta M/M$  of about 6%. Angular distributions are shown in Fig. 6 for the  $^{28}\text{Si}+^{28}\text{Si}$  exit-channel. The  $\gamma$  rays emitted by the fragments were detected by the EURO-GAM Phase II multidetector array [49], composed of 54 Compton-suppressed germanium (Ge) detectors with 30 large volume tapered coaxial Ge detectors (from EURO-GAM Phase I [54]) located in both the

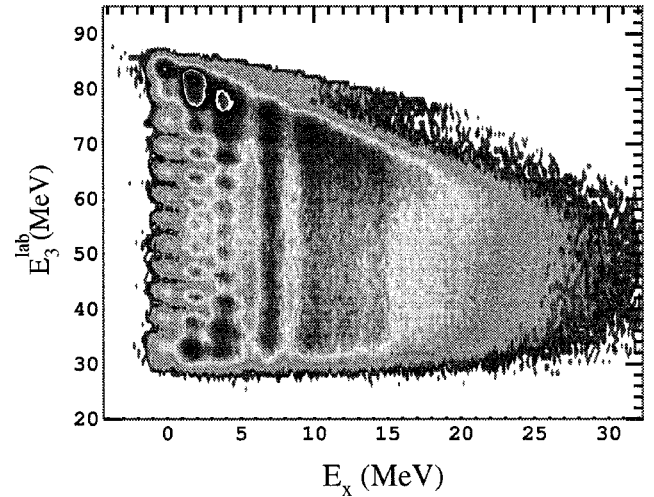


FIG. 2. Ejectile energy  $E_3$  versus excitation energy  $E_x$  two-dimensional plot of the  $^{28}\text{Si}+^{28}\text{Si}$  symmetric-mass exit channel.

forward and the backward hemispheres, and 24 Clover Ge detectors [55] located around  $\sim 90^\circ$  relative to the beam axis. The number of Ge crystals at each angle with respect to the beam direction was (5,  $22^\circ$ ), (10,  $46^\circ$ ), (24,  $71^\circ$ ), (24,  $80^\circ$ ), (24,  $100^\circ$ ), (24,  $109^\circ$ ), (10,  $134^\circ$ ), and (5,  $158^\circ$ ). The electronics used for the PSD's consisted of VXI germanium cards from EURO-GAM. Events were recorded with the condition that at least one of the two PSD pairs fired in coincidence (start) with  $\gamma$  rays detected in EURO-GAM. Doppler-shift corrections were applied to the  $\gamma$ -ray data on an event-by-event basis [56]. The energy and relative efficiency

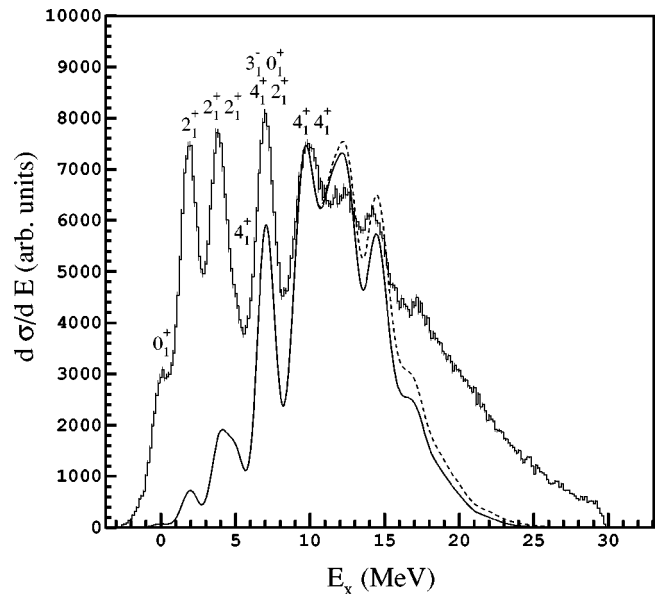


FIG. 3. Excitation-energy spectrum for the  $^{28}\text{Si}+^{28}\text{Si}$  exit channel measured at large angles. Tentative assignments of the resolved and nonresolved peaks are indicated. The bold-line histograms are efficiency corrected (absolute) cross sections. The lighter curves are the results of the TSM calculations discussed in the text for fission decay to particle-bound (solid curve) and for all decays (dotted curve).

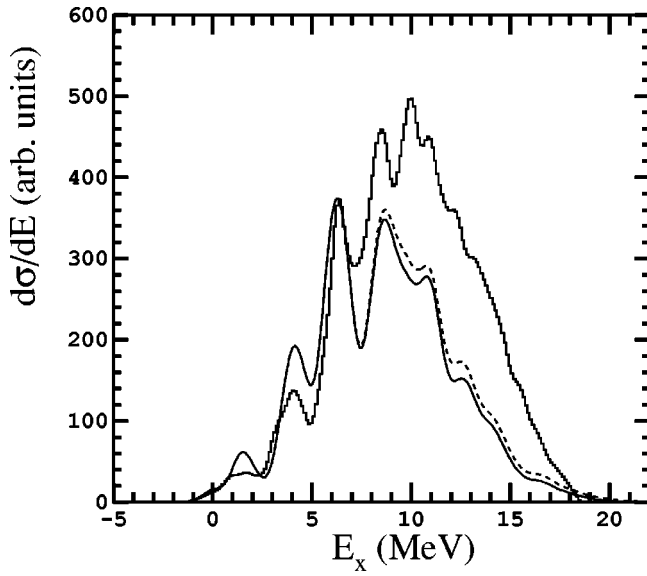


FIG. 4. Excitation-energy spectrum for the  $^{32}\text{S} + ^{24}\text{Mg}$  exit channel measured at large angles. The bold-line histograms are efficiency corrected (relative) cross sections. The curves which are defined in the same manner as in Fig. 3 have been normalized to the experimental cross sections.

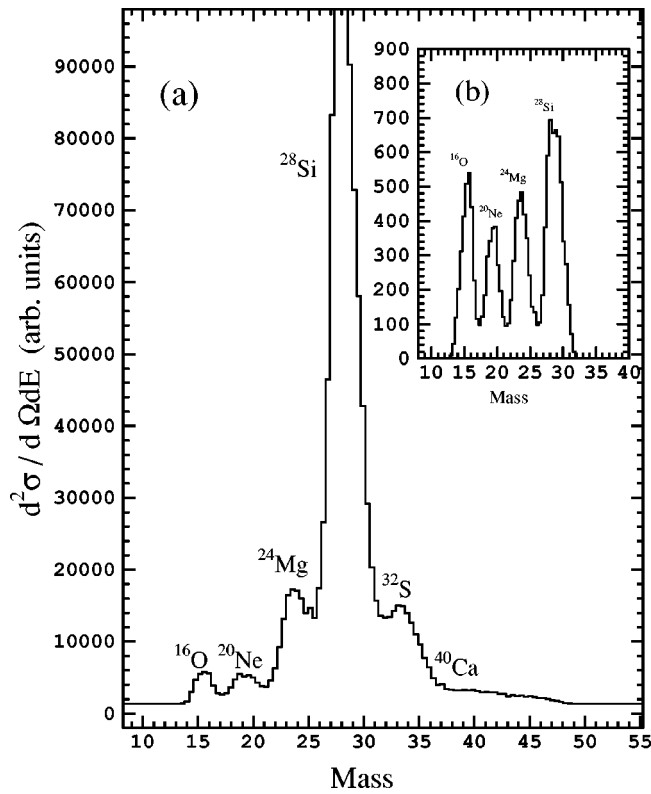


FIG. 5. Mass distribution based on the coincident detection of the binary fragment  $M_3$  in region 1 as defined in the text. (a) Corresponds to the  $^{28}\text{Si} + ^{28}\text{Si}$  exit channel; (b) corresponds to products arising from a reaction of the  $^{28}\text{Si}$  projectile on the  $^{16}\text{O}$  contamination.

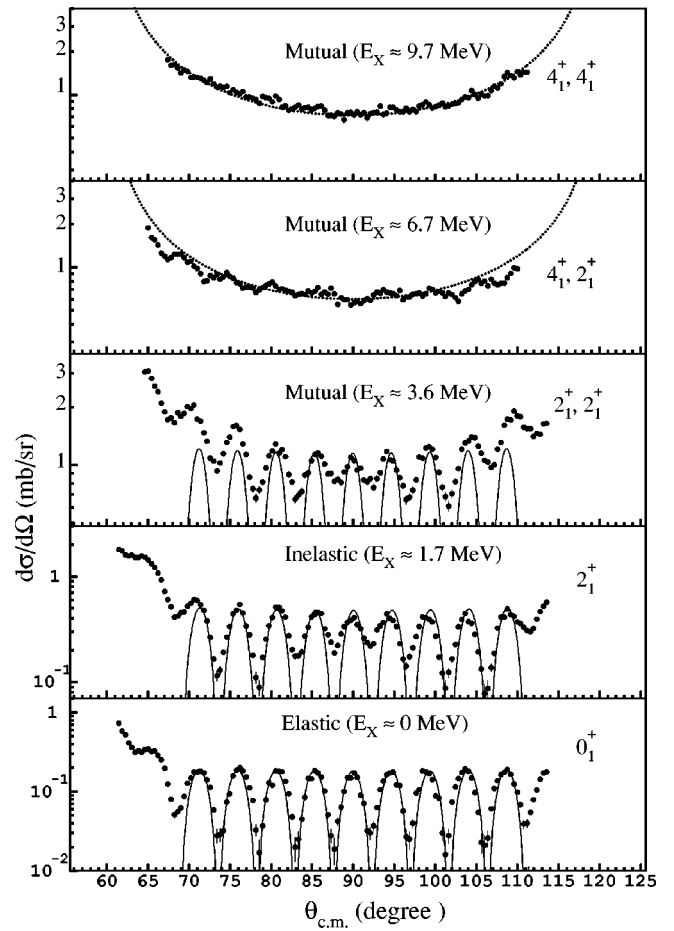


FIG. 6. Experimental angular distributions of the elastic, inelastic  $2_1^+$  and mutual ( $2_1^+, 2_1^+$ ), and higher excitation channels ( $E_X = 6.7$  and  $8.7$  MeV). The solid lines are  $[P_L(\cos \theta)]^2$  curves for  $L = 38\hbar$ . The dotted curves correspond to a  $1/\sin \theta_{c.m.}$  behavior. The  $\chi^2$  results as a function of  $L$  are given in the insert for the elastic scattering.

calibrations of the Ge detectors were obtained using standard  $\gamma$ -ray sources located at the target position with the scattering chamber in place. The higher energy  $\gamma$ -ray region (up to  $E_\gamma = 7630$  and  $7648$  keV, a doublet in  $^{57}\text{Fe}$ ) was calibrated with an AmBe source. Above this energy the efficiency was extrapolated, based on the smooth exponential behavior exhibited by the calibration at lower energies. Coincident  $\gamma$ -ray spectra are displayed in Figs. 7, 8, and 9 for three different exit channels.

### III. FRAGMENT-FRAGMENT COINCIDENCE RESULTS

The exclusive data as obtained by the fragment-fragment coincidence measurements are illustrated in Fig. 1 by a typical two-dimensional energy spectrum  $E_3$ - $E_4$  of the binary fragments detected in coincidence with one pair of PSD's in the angular ranges of  $23.3^\circ \leq \theta_3 \leq 70.9^\circ$  and  $22.1^\circ \leq \theta_4 \leq 73.3^\circ$ , respectively.  $E_3$ ,  $E_4$ ,  $\theta_3$ , and  $\theta_4$  are the energies and positions of the two fragments detected in coincidence. The symmetry of this spectrum reflects the nearly symmetric configuration of the experimental setup. Three different re-

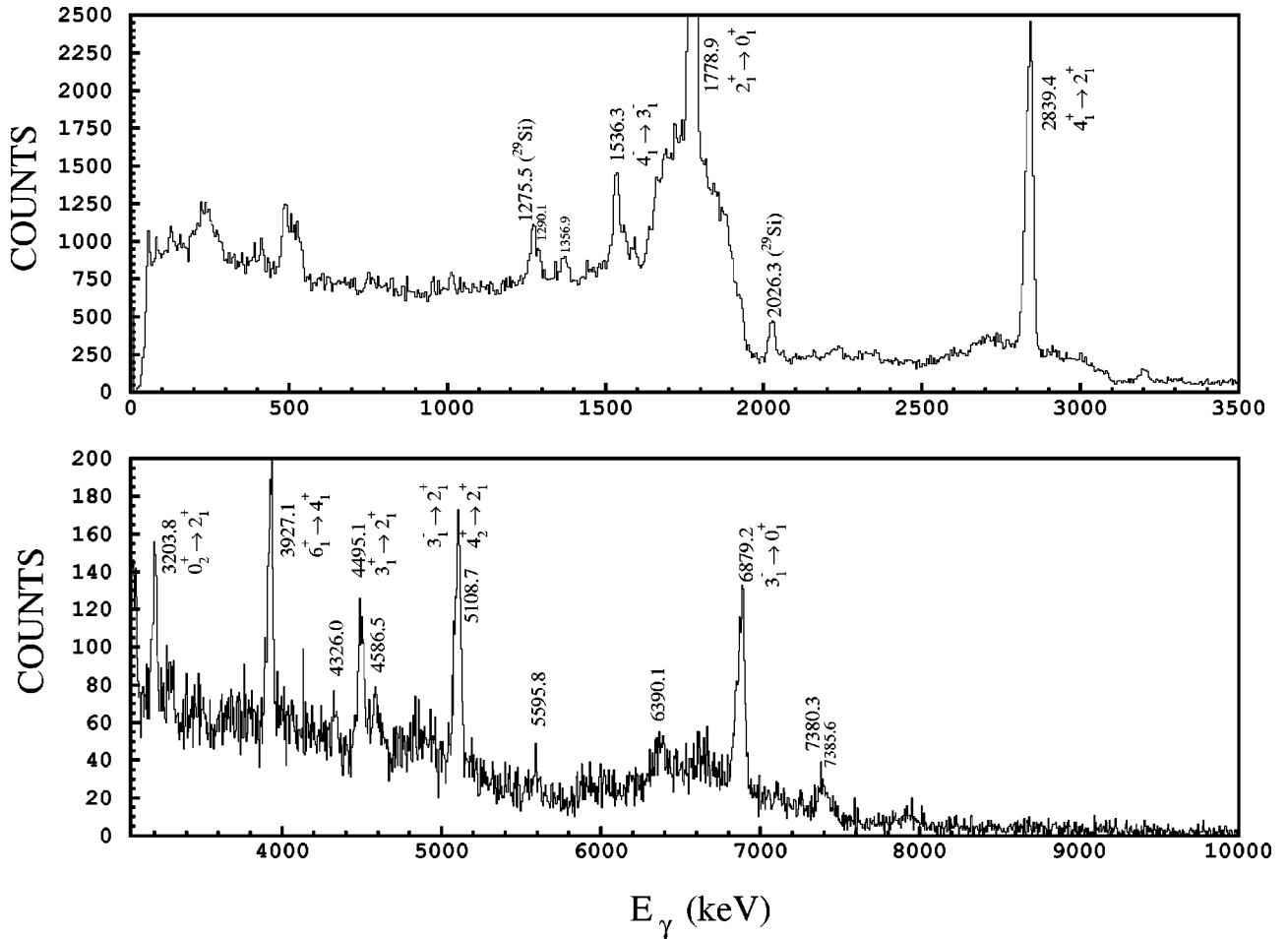


FIG. 7.  $\gamma$ -ray spectrum in coincidence with the  $^{28}\text{Si}+^{28}\text{Si}$  symmetric mass exit-channel. Doppler-shift corrections have been applied according to mass  $M_3=28$ .

regions can be distinguished: these are marked in Fig. 1. Region 1 corresponds to binary products arising mainly from the  $^{28}\text{Si}+^{28}\text{Si}$  reaction of interest (reaction products from scattering on lighter-mass target contamination such as O are also present as is shown more clearly in Fig. 5). In this region the angular distributions of the low-energy states are well structured as expected at the resonance energy. Region 2 of Fig. 1 arises from the reaction products of  $^{28}\text{Si}$  incident on a heavier-mass target contaminant (such as  $^{63}\text{Cu}$ ), and region 3 corresponds to the light charged particle ( $p$ ,  $\alpha$ ) coincidences arising primarily from the fusion evaporation of the  $^{56}\text{Ni}$  compound system. In the following only the events belonging to region 1 will be considered for the analysis. The selection of the different exit channels was done using mass spectra constructed using standard binary kinematics relations [50–53]. An example of the fragment mass distributions ( $M_3$  being the ejectile mass) is displayed in Fig. 5. The figure shows that region 1 is formed by two kinds of reactions. The first reaction [as illustrated in Fig. 5(a)] corresponds to binary products of  $^{28}\text{Si}+^{28}\text{Si}$  at the resonance energy, and shows that the reaction is dominated by the  $^{28}\text{Si}+^{28}\text{Si}$  symmetric mass exit channel. This reflects the PSD's locations which have been optimized to study this exit channel. The second reaction [see Fig. 5(b)] arises from the reac-

tion  $^{28}\text{Si}$  on the  $^{16}\text{O}$  target contaminant. These contaminant events have been selected by making use of the compound system mass deduced from the coincidence measurement.

The reaction  $Q$ -value spectra were obtained for the different binary-reaction channels based on the known entrance-channel parameters, the deduced mass of the fragments ( $M_3$  and  $M_4$ ), the total mass of the compound system ( $M_T$ ), and the observed fragment angles and kinetic energies [52,53]. The  $Q$  values were then converted to excitation energies ( $E_X$ ) of the binary products using  $E_X = Q_{gg} - Q^* = Q_{gg} + E_{\text{lab}} - (E_3 + E_4)$  where  $Q_{gg}$  is the reaction  $Q$  value. Figure 2 displays the mass-gated ( $M_3=28$ ) two-dimensional spectrum of the ejectile energy  $E_3$  as a function of the calculated excitation energy ( $E_X$ ) for the  $^{28}\text{Si}+^{28}\text{Si}$  symmetric mass exit channel. The vertical bands correspond to different excited states in the two  $^{28}\text{Si}$  fragments, where the regular concentrations of yields are due to strongly structured angular distributions which will be analyzed in Sec. III B. The excitation-energy spectra are first presented in the following section.

#### A. Excitation-energy spectra

Excitation-energy spectra were generated for the  $^{28}\text{Si}+^{28}\text{Si}$  exit channel (Fig. 3) and the  $^{32}\text{S}+^{24}\text{Mg}$  exit channel

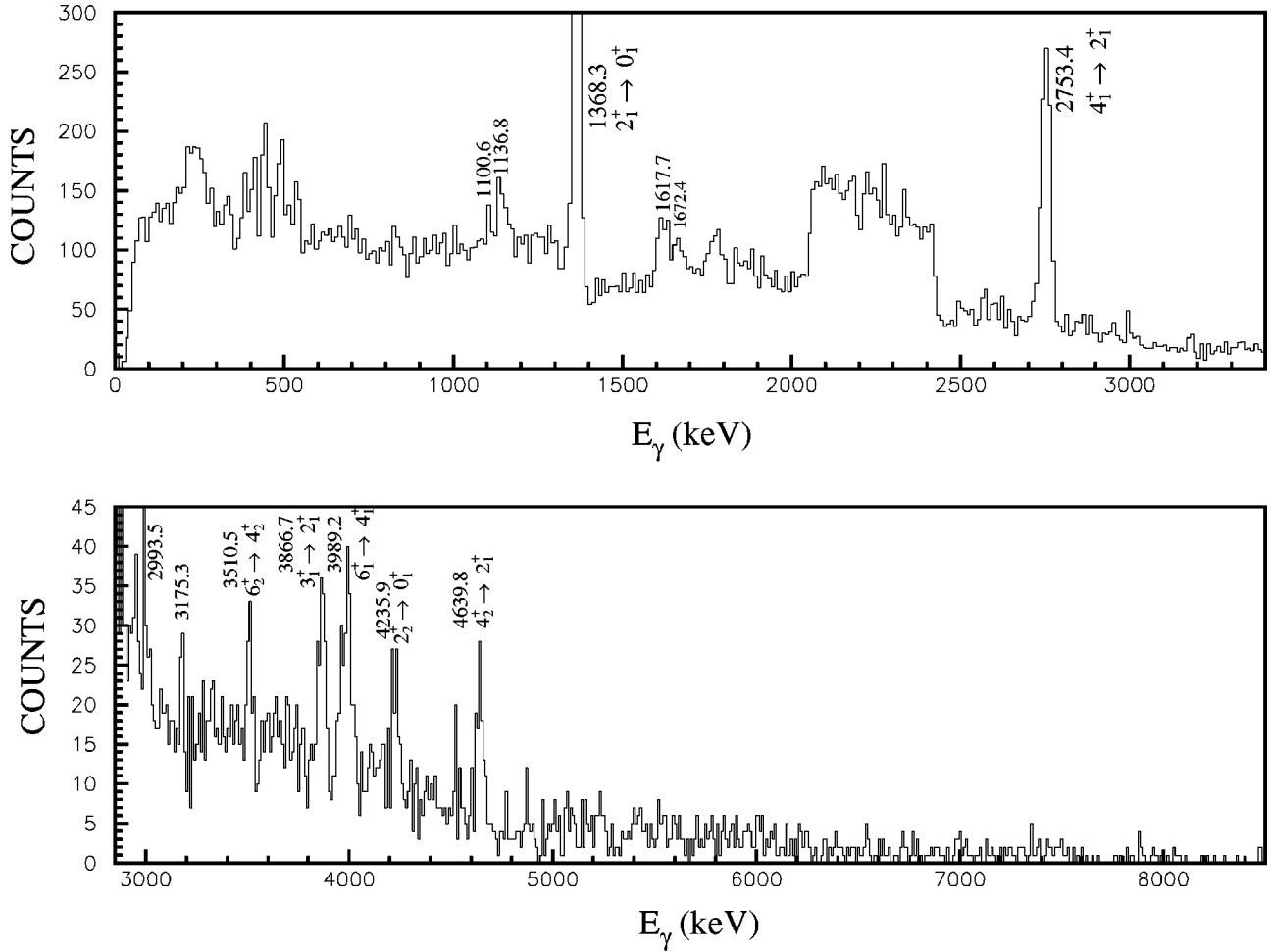


FIG. 8.  $\gamma$ -ray spectrum for the  $^{32}\text{S}+^{24}\text{Mg}$  near symmetric mass exit channel measured in coincidence with  $^{24}\text{Mg}$  fragments. Doppler-shift corrections have been applied according to mass  $M_3=24$ .

(Fig. 4), respectively, by setting mass gates with  $M_3=28$  and 32 (24) while requiring a calculated total mass of  $M_T=56$ . The detection efficiency for the two mass channels was determined on an event-by-event basis from a simple simulation program of the fragment-fragment coincidence arrangement [52]. The resolution in the experimental excitation-energy spectra and, in particular, the resolving power provided by the  $\gamma$  rays in determining the  $^{28}\text{Si}$  final states has already been described in our previous Rapid Communication [47].

The excitation-energy spectrum for the  $^{28}\text{Si}+^{28}\text{Si}$  symmetric mass exit channel, displayed in Fig. 3, exhibits a very striking and well structured behavior up to high excitation energy ( $E_X \approx 15$  MeV). The low excitation-energy peaks correspond to the elastic scattering and inelastic scattering to low lying states of  $^{28}\text{Si}$  (mainly the 1.78 MeV  $2_1^+$  state, and the weaker 4.62 MeV  $4_1^+$  state which yields the shoulder of the  $2^+$  peak). The strong peaks observed at more negative  $Q$  values more likely arise from mutual excitations. The level assignments for the higher  $E_X$  peaks are speculative, although the locations of these peaks are consistent with mutual excitation of yrast states in both fragments, as suggested previously [9,50]. The observation that both fragments have

quite high spins is consistent with a simple sticking picture of the deep-inelastic (DI) collision process [24] in which the two colliding  $^{28}\text{Si}$  nuclei have adhered to each other, rotated, and then separated again. This process transforms orbital angular momentum into fragment spin with a substantial loss in the kinetic energy associated with relative motion. In other words, the large angle cross sections suggest the formation and decay of a long-lived dinuclear system (i.e., a nuclear molecule) which scissions at quite large deformations. The alternative explanation involves a FF origin in which the system forms an equilibrated CN before its subsequent binary decay [24]. It has been previously shown for the  $^{32}\text{S}+^{24}\text{Mg}$  reaction [31] that much of the structure seen in the excitation-energy spectra can be understood in terms of the statistical population of levels in the fragments. Thereafter the same statistical model calculation will be used to generate an excitation-energy spectrum to be compared with the present data. The large cross sections associated with low excitation energies, however, appears to be of a nonstatistical origin and most likely reflect the resonant nature of the system. This will be discussed in more detail in the analysis of the  $\gamma$ -ray coincident results in Sec. IV.

For the  $^{32}\text{S}+^{24}\text{Mg}$  exit channel [56] the more pronounced structures are observed at higher excitation energies

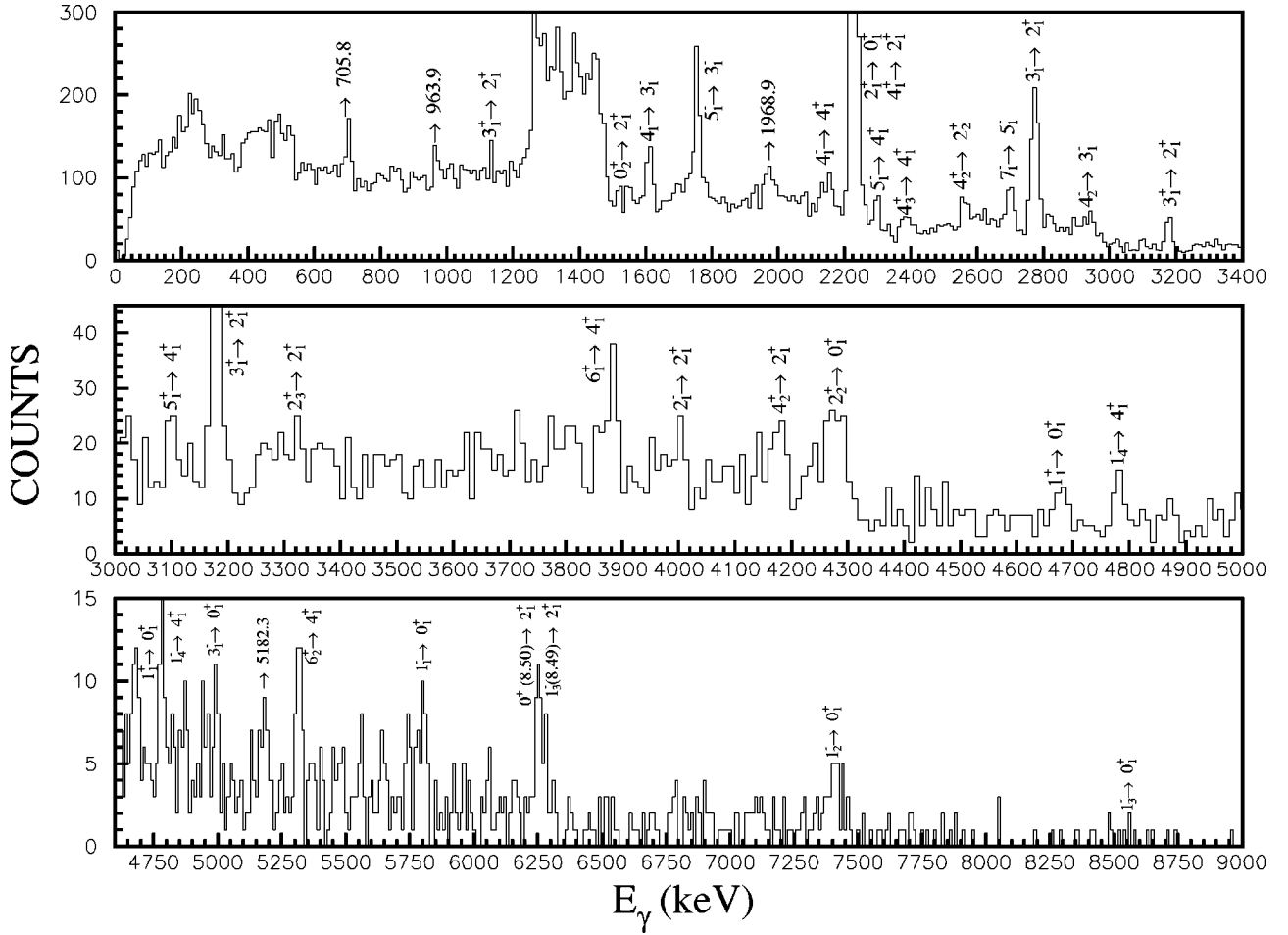


FIG. 9.  $\gamma$ -ray spectrum for the  $^{32}\text{S}+^{24}\text{Mg}$  near symmetric mass exit channel measured in coincidence with  $^{32}\text{S}$  fragments. Doppler-shift corrections have been applied according to mass  $M_3=32$ .

( $6 \text{ MeV} \leq E_X \leq 10 \text{ MeV}$ ), as seen in Fig. 4. Previous measurements for the  $^{28}\text{Si}+^{28}\text{Si} \rightarrow ^{32}\text{S}+^{24}\text{Mg}$  reaction have not shown evidence for resonancelike behavior [31]. Our excitation-energy spectrum is in qualitative agreement with this observation as very little strength is seen in the low-lying states. The observed yield to these states may be attributed to a fusion-fission mechanism. A comprehensive statistical-model analysis of both exit channels will be given in Sec. V.

### B. Angular distributions for the $^{28}\text{Si}+^{28}\text{Si}$ exit channel

The angular distributions, shown in Fig. 6 for the symmetric-mass exit channels, have been deduced from projections onto the  $E_3$  axis with excitation energy gates as defined by the states of Fig. 2. The elastic, inelastic  $2_1^+$ , and mutual inelastic ( $2_1^+, 2_1^+$ ) channels display strongly oscillatory angular distributions at backward angles (between  $70^\circ \leq \theta_{\text{c.m.}} \leq 110^\circ$ ). The angular distribution of the elastic scattering data [6] at a bombarding energy corresponding roughly to twice the Coulomb barrier, shows at forward angles a typical transition from Coulomb scattering through nuclear-Coulomb interference, to a steep and smooth fall off beyond the grazing angle ( $\theta_{\text{c.m.}} \approx 44^\circ$  as deduced from a quarter-point analysis of the elastic scattering [57]), charac-

teristic of the scattering of strongly absorbing particles. These features are readily described in a variety of OM calculations. A typical OM analysis of the  $^{28}\text{Si}+^{28}\text{Si}$  elastic scattering has been performed at the bombarding energy of  $E_{\text{lab}}=120 \text{ MeV}$  using a strongly absorbing potential [6]. The results of the comparison can be found in Refs. [2,6]. At the largest angles, however, the present data show an abrupt transition to the highly oscillatory behavior associated with weak absorption, in accordance with NOC [21,22] predictions. The elastic cross sections observed in this angular region are from one to three orders of magnitude (near  $\theta_{\text{c.m.}}=90^\circ$ ) larger than those obtained from OM calculations using standard strongly absorbing potential parameters [6,57] which give a good account of the data forward of  $\theta_{\text{c.m.}}=70^\circ$ . This behavior suggests the presence of a significantly slower reaction mechanism than the direct and multistep processes which dominate at more forward angles ( $\theta_{\text{c.m.}} \leq 70^\circ$ ).

The present back-angle, high-quality elastic and inelastic-scattering data, with good angular (position) resolution and high statistics, are well described by a  $P_L^2(\cos \theta_{\text{c.m.}})$  angular dependence with  $L=38$ , in agreement with the older data of Betts *et al.* [8]. This behavior can be understood if these distributions are dominated by a single partial wave, or by a

few partial waves that are in phase. The analysis of angular distribution data for resonance parameters can lead to ambiguities when the nonresonant “background” amplitudes are not fully known. To explore this issue, a phase-shift analysis [58] of the present elastic scattering data is carried out separately. Still, the elastic data shown in Fig. 6 strongly suggest an  $L=38$  assignment for the resonant state.

For the mutual inelastic ( $2_1^+$ ,  $2_1^+$ ) channel, the regular and periodic oscillations still persist in the angular distribution data. Again, the analysis suggests that the largest contribution is from  $L=38$ , with possibly smaller contributions of  $L=36$  and  $40$ , as discussed in our earlier Rapid Communication [47]. The small shifts of the oscillation maxima may be explained by the larger nonresonant backgrounds in this channel due to FF and/or DI orbiting contributions. The dominance of the orbital angular momentum  $L=38$  in the three resonant channels implies that the projection of the final channel spin along the direction perpendicular to the reaction plane is  $m=0$ . This unexpected spin “disalignment” is confirmed by the analysis of the angular correlation of the  $\gamma$ -rays, as presented in Ref. [47] and summarized in Sec. IV C.

It should be noted that the angular momenta values (from  $36\hbar$  to  $40\hbar$ ) suggested by the data are significantly larger than the critical angular momentum for fusion. Based on the available  $^{28}\text{Si}+^{28}\text{Si}$  complete fusion (CF) data [57,59], a value  $L_{\text{crit}}\approx 35\hbar$  is obtained. The grazing angular momentum  $L_{\text{graz}}\approx 38\text{--}40\hbar$  is obtained from a quarter point analysis of the elastic scattering data [57]. At such high angular momenta the  $^{56}\text{Ni}$  CN is near the point where the fission barrier vanishes [23], highlighting the large deformations which are induced during the scattering process.

The angular distribution of the mutual excitation states ( $4_1^+$ ,  $2_1^+$ ) at an excitation energy  $E_X\approx 6.7$  MeV is not as strongly structured as the lower-energy channels. This is presumably due to a larger number of contributing partial waves. The angular distribution, also displayed in Fig. 6, for mutual excited states ( $4_1^+$ ,  $4_1^+$ ) has a shape comparable to  $1/\sin\theta_{\text{c.m.}}$ , suggestive of the emission of the two  $^{28}\text{Si}$  fragments in a fully relaxed process such as FF and/or DI orbiting contributions.

In the back-angle region, the elastic scattering channel is relatively weak as compared to the inelastic and mutual inelastic channels, as seen in Fig. 3. These excited channels show the same general angular behavior as the elastic channel; namely, a forward angle dependence of the cross-section characteristic of Coulomb and nuclear scattering with strong absorption (see the complete angular distributions measured at  $E_{\text{lab}}=120$  MeV [11] and unpublished data at  $E_{\text{lab}}=112$  MeV from Betts *et al.* [2]), and a back-angle behavior suggesting the presence of a process with much longer time scale. The total cross section for the  $^{28}\text{Si}+^{28}\text{Si}$  exit-channel can be estimated from the excitation energy spectra and is found to be  $7\pm 3$  mb, i.e., approximately 1% of the total CF cross section [57,59]. FF calculations using either the transition-state model [33] (TSM) or the extended Hauser-Feshbach method [34] predict approximately 5–6 mb for the symmetric-mass fission cross section, in good agreement

with the observed yield. It should be noted that FF models [33,34] do not include a resonance contribution. The significantly enhanced yield at low excitation energy in the  $^{28}\text{Si}+^{28}\text{Si}$  exit channel as compared to FF calculations may reflect in part contribution to the yields of an additional resonance component.

To summarize this analysis, the angular distribution data show that the measured back-angle yields for the three low-lying states are characterized, to a large extent, by a resonance behavior. The FF process is believed to dominate the yields at higher excitation energies ( $E_X\geq 6$  MeV), as discussed further in Sec. V with respect to the TSM calculations.

#### IV. FRAGMENT-FRAGMENT-GAMMA COINCIDENCE RESULTS

In this section we will focus on the analysis of the fragment-fragment- $\gamma$  coincidence data for the  $^{28}\text{Si}+^{28}\text{Si}$  mass-symmetric exit channel and for the  $^{32}\text{S}+^{24}\text{Mg}$  near symmetric exit channel.

##### A. Coincident $\gamma$ -ray spectra

###### 1. Feeding of $^{28}\text{Si}$ states

The  $\gamma$ -ray spectrum measured in coincidence with both  $^{28}\text{Si}$  fragments, without any condition on the angles between the particles, is displayed in Fig. 7. Since it is not possible to know which of the two  $^{28}\text{Si}$  fragments emits the detected  $\gamma$  ray, both Doppler corrections were applied by using the method developed in Refs. [31,36]. Some Doppler broadening of the  $\gamma$ -ray lines is still present due to the finite angular acceptance of the Ge detectors and finite position resolution of the PSD's. The  $\gamma$ -ray peak width, for example, changes from  $\approx 10$  keV at 1779 keV (the broad peak beneath the 1779 keV  $\gamma$ -ray transition is due to the wrong Doppler correction) to  $\approx 32$  keV at 5110 keV. Some of the stronger transitions are labeled by their energy in keV, and by the initial and final levels, spins and parities.

In order to investigate the resonant effects on the feeding of the  $^{28}\text{Si}$  states, and to search for possible highly deformed bands in  $^{28}\text{Si}$ , we have generated  $\gamma$  spectra for two different angular regions of the particle angular distribution shown in Fig. 6. The first region, with  $73.2^\circ\leq\theta_{\text{c.m.}}\leq 105.6^\circ$ , is where the angular distributions oscillate strongly (see Fig. 6). In the following this is referred to as the “large-angle region.” The second region is defined as the “directlike region” and is in the  $56.8^\circ\leq\theta_{\text{c.m.}}\leq 67.6^\circ$  angular range. The main  $\gamma$ -ray transitions in  $^{28}\text{Si}$ , as observed in the “large-angle region,” are listed in Table I, with their relative intensities. The feeding of the known  $^{28}\text{Si}$  states [60–64] in both the “large-angle region” and the “directlike region” have been deduced following the procedure proposed in Ref. [31], where a detailed level scheme of the  $^{28}\text{Si}$  nucleus, including its complete band structure, is presented (see Fig. 15 of Ref. [31]). The  $\gamma$ -ray transitions observed in the  $^{29}\text{Si}$  and  $^{27}\text{Al}$  (not listed in Table I) nuclei confirm that the mass identification provided by Fig. 5 was not perfect.

TABLE I.  $\gamma$ -ray transitions observed in coincidence with two  $^{28}\text{Si}$  fragments detected in the ‘‘large-angle region.’’ Initial and final spins, and the excitation energies of the levels emitting the  $\gamma$  ray are given in the first columns. The efficiency corrected  $\gamma$ -ray yields (given by their relative intensities) measured in the ‘‘large-angle region’’ and in the ‘‘directlike’’ region, respectively, and normalized to the  $2_1^+ \rightarrow 0_1^+$  1778.9 keV transition, are given in the last two columns.

$E_\gamma^{\text{exp}}$ (keV)	$\gamma$ -ray transition	$E_{\text{lev}}^*$ (keV)	$I_\gamma^{\text{larg}}$ (%)	$I_\gamma^{\text{dir}}$ (%)
1275.5	$^{29}\text{Si}$	1273.3		
1289.2	$5_1^- \rightarrow 4_1^-$	9702.3	1.05(0.29)	
1364.3	$^{24}\text{Mg}$	1368.7		
1534.0	$4_1^- \rightarrow 3_1^-$	8413.3	6.09(0.60)	8.52(2.41)
1594.2	$^{29}\text{Si}$	1595.3		
1778.9	$2_1^+ \rightarrow 0_1^+$	1778.9	100(1.01)	100(1.76)
1875.0	$6_1^- \rightarrow 5_1^-$	11576.8	3.40(0.87)	
2026.3	$^{29}\text{Si}$	2028.2		
2823.9	$5_1^- \rightarrow 3_1^-$	9702.3	0.54(0.15)	
2837.2	$4_1^+ \rightarrow 2_1^+$	4617.8	21.4(0.73)	22.1(0.97)
3199.8	$0_2^+ \rightarrow 2_1^+$	4979.9	1.25(0.26)	1.46(0.38)
3310.8	$5_2^- \rightarrow 3_1^-$	10189.6	0.61(0.28)	0.33(0.15)
3925.4	$6_1^+ \rightarrow 4_1^+$	8543.5	4.14(0.44)	4.36(0.72)
4495.7	$3_1^+ \rightarrow 2_1^+$	6276.2	2.59(0.32)	1.30(0.44)
4596.9	$2_2^+ \rightarrow 2_1^+$	7380.8		0.66(0.22)
4623.0	$6_3^+ \rightarrow 4_2^+$	11509.1	0.48(0.33)	
4915.1	$0_3^+ \rightarrow 2_1^+$	6691.4	0.21(0.05)	
5084.0	$5_1^- \rightarrow 4_1^-$	9702.3	0.36(0.09)	
5101.2	$3_1^- \rightarrow 2_1^-$	6878.7	1.00(0.17)	1.40(0.23)
5107.3	$4_2^+ \rightarrow 2_1^+$	6887.6	3.47(0.18)	3.89(0.25)
6476.1	$2_5^+ \rightarrow 2_1^+$	8258.7	0.29(0.10)	
6631.4	$4_1^- \rightarrow 2_1^-$	8413.3	1.29(0.12)	0.46(0.17)
6879.4	$3_1^- \rightarrow 0_1^-$	6878.7	5.90(0.51)	4.28(0.74)
7123.9	$1_1^- \rightarrow 2_1^-$	9929.2	0.29(0.07)	0.47(0.19)
7380.3	$2_2^+ \rightarrow 0_1^+$	7380.8		
7385.6	$4_3^+ \rightarrow 2_1^+$	9164.6	2.12(0.42)	
7415.0	$2_3^+ \rightarrow 0_1^+$	7416.3		
7922.7	$5_1^- \rightarrow 2_1^-$	9702.3	0.24(0.04)	
7938.7	$2_4^+ \rightarrow 0_1^+$	7933.4	0.87(0.34)	

The comparison of the measured feeding of  $^{28}\text{Si}$  states in the ‘‘large-angle region’’ and the ‘‘directlike region’’ is illustrated in Figs. 10 and 11, respectively. The feeding of the  $K^\pi = 3_1^-$  and  $5_1^-$  oblate bands is found to be stronger in the ‘‘large-angle region,’’ in contrast to that of the  $K^\pi = 3_1^+$  prolate band. A quantitative comparison is summarized in Table II, where the relative feeding of  $K^\pi$  bands are defined as follows:

$$\mathcal{R}(K^\pi) = \frac{\mathcal{A}(K^\pi)}{\mathcal{A}(K^\pi = 0_1^+)}, \quad (1)$$

where  $\mathcal{A}(K^\pi)$  is the feeding of a  $K^\pi$  band of  $^{28}\text{Si}$ .

The results presented in Fig. 10 indicate that the  $K^\pi = 3_1^-$  band is strongly fed as indicated by the strong popula-

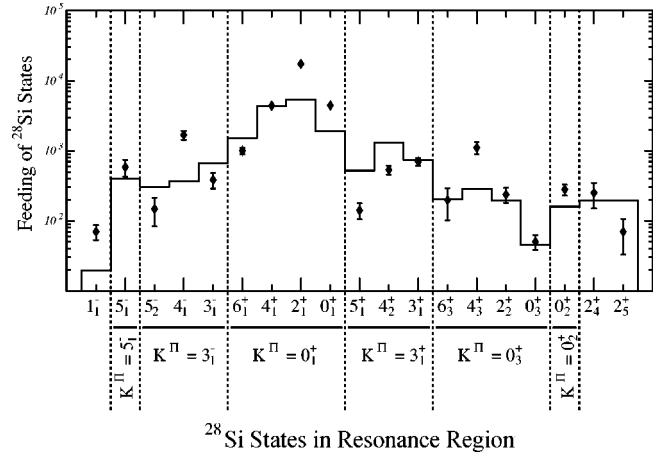


FIG. 10. Comparison between measured feedings and calculated (diamonds and triangles) for states in  $^{28}\text{Si}$  as populated in the ‘‘large-angle region.’’ The calculated feedings have been obtained with the TSM (histograms) for a statistical FF process described in the text.

tion of the  $4_1^-$  state. The population of the 6.88 MeV collective  $3_1^-$  state, which was not apparent in the present fragment-fragment coincidence data of Fig. 3 nor in previous high resolution studies [8,9,50], is quite strong. This is an indication that the  $^{28}\text{Si}$  nucleus has an oblate deformed shape when the resonant features are present. Model predictions [73] applied to the  $^{28}\text{Si} + ^{28}\text{Si}$  elastic scattering, in which the excited states of the individual interacting surfaces, including the  $3_1^-$  excitation of  $^{28}\text{Si}$ , constitute the vibrations, support also the association of the resonance with nuclear molecule formation [73].

As previously found in a study of the  $^{24}\text{Mg}(^{32}\text{S}, ^{28}\text{Si})^{28}\text{Si}$  reaction [31], states belonging to the second excited band  $K^\pi = 0_3^+$  appear to be strongly populated. A comparison of the observed population with that expected based on the statistical population of  $^{28}\text{Si}$  states within the framework of the transition-state model (TSM) is presented in Sec. V A.

The population of the ground state  $K^\pi = 0_1^+$  band indicates that the mutually excited states are more intensely fed

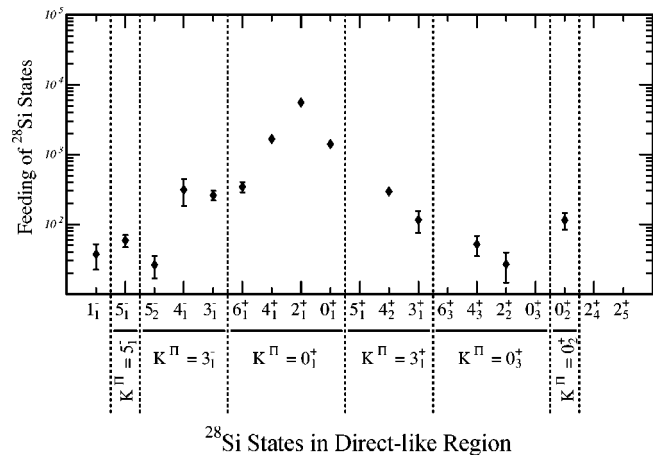


FIG. 11. Experimental feedings (diamonds) for states in  $^{28}\text{Si}$  as populated in the ‘‘directlike region.’’

TABLE II. Relative feedings (in percentage) of  $K^\pi$  bands [ $\mathcal{R}(K^\pi)$ ] for states in  $^{28}\text{Si}$  populated in the ‘‘large-angle region’’ and in the ‘‘directlike region,’’ respectively.

$K^\pi$	$5_1^-$	$3_1^-$	$0_1^+$	$3_1^+$	$0_3^+$	$0_2^+$
Kind of deformation	large oblate deformation	oblate deformation	oblate deformation	prolate deformation	large prolate deformation	prolate deformation
$\mathcal{R}(K^\pi)$						
‘‘large-angle region’’	$2.1 \pm 0.4$	$8.2 \pm 0.7$	100	$4.4 \pm 0.5$	$5.8 \pm 1.1$	$1.2 \pm 0.4$
$\mathcal{R}(K^\pi)$						
‘‘directlike region’’	$0.7 \pm 0.3$	$6.7 \pm 0.8$	100	$4.5 \pm 0.4$	$1.1 \pm 0.7$	$1.3 \pm 0.4$

than the singly excited states ( $0_1^+$ ,  $0_1^+$ ), ( $2_1^+$ ,  $0_1^+$ ), and ( $4_1^+$ ,  $0_1^+$ ). This high degree of selectivity in the population of mutually excited yrast states in both  $^{28}\text{Si}$  fragments confirms the early findings of Betts *et al.* [9].

The strong populations found for the  $K^\pi = 3_1^-$ ,  $5_1^-$ , and  $0_1^+$  bands implies that  $^{28}\text{Si}$  is dominated by oblate deformation. Perhaps more interesting are the observations that the  $K^\pi = 0_3^+$  band, corresponding to the large prolate deformation, is more strongly populated in the ‘‘large-angle region’’ than in the ‘‘direct-like region’’ by a factor 6, and that the  $K^\pi = 5_1^-$  band corresponding to the large oblate deformation is three times more strongly fed in the ‘‘large-angle region.’’

## 2. $\gamma$ -ray spectroscopy of the $^{24}\text{Mg}$ and $^{32}\text{S}$ nuclei

The  $\gamma$ -ray spectra observed in coincidence with the  $^{24}\text{Mg}$  and  $^{32}\text{S}$  fragments at high excitation-energy ( $E_X > 10$  MeV) are displayed in Figs. 8 and 9. The main  $\gamma$ -ray transitions in  $^{24}\text{Mg}$  and  $^{32}\text{S}$  are listed in Tables III and IV, respectively. Again, since it is not possible to determine which of the two fragments emits the  $\gamma$  ray, both Doppler-shift corrections have been applied. Figure 8 assumes that the  $\gamma$  ray is emitted from the  $^{24}\text{Mg}$  nucleus, whereas Fig. 9 assumes emission from the  $^{32}\text{S}$  nucleus. The large bump observed at  $E_\gamma \approx 2100$ – $2400$  keV (1250–1450 keV) for the  $^{24}\text{Mg}$  ( $^{32}\text{S}$ )  $\gamma$ -ray spectrum of Fig. 8 (Fig. 9) corresponds to

TABLE III.  $\gamma$ -ray transitions in coincidence with  $^{24}\text{Mg}$  in the  $^{32}\text{S} + ^{24}\text{Mg}$  exit channel. The efficiency corrected  $\gamma$ -ray yields (given by their relative intensities), normalized to the  $2_1^+ \rightarrow 0_1^+$  1368.6 keV transition, are given in the last column.

$E_\gamma^{\text{exp}}$ (keV)	$\gamma$ -ray transition	$E_{\text{level}}^*$ (keV)	$I_\gamma$ (%)
1368.3	$2_1^+ \rightarrow 0_1^+$	1368.6	100(2.5)
1769.8	$4_2^+ \rightarrow 2_2^+$	6010.3	0.82(0.2)
2753.4	$4_1^+ \rightarrow 2_1^+$	4122.8	3.99(2.3)
3510.5	$6_2^+ \rightarrow 4_2^+$	9528.0	4.17(0.7)
3866.7	$3_1^+ \rightarrow 2_1^+$	5236.1	6.67(1.1)
3989.2	$6_1^+ \rightarrow 4_1^+$	8113.0	8.22(1.2)
4235.9	$2_2^+ \rightarrow 0_1^+$	4236.4	4.05(0.9)
4639.8	$4_2^+ \rightarrow 2_1^+$	6010.3	5.54(1.0)
5230.2	$3_1^+ \rightarrow 0_1^+$	5236.1	0.65(0.2)
5412.1	$6_2^+ \rightarrow 4_1^+$	9528.0	1.13(0.4)
7350.3	$2_3^+ \rightarrow 0_1^+$	7347.9	0.74(0.2)

the incorrect Doppler-shift correction of the  $2^+ \rightarrow$  g.s. transition of the  $^{32}\text{S}$  ( $^{24}\text{Mg}$ ) recoil.

Remarkably, the  $\gamma$ -ray spectrum of  $^{24}\text{Mg}$  (Fig. 8) shows exclusively  $\gamma$ -ray transitions between positive-parity states, with no transitions observed between negative-parity levels. This property may be linked to the specific nature of  $^{24}\text{Mg}$  which, in its ground state, has a prolate shape. The  $^{24}\text{Mg}$  nucleus appears to be populated primarily through its first

TABLE IV.  $\gamma$ -ray transitions in coincidence with  $^{32}\text{S}$  in the  $^{32}\text{S} + ^{24}\text{Mg}$  exit channel. The efficiency corrected  $\gamma$ -ray yields (given by their relative intensities), normalized to the  $2_1^+ \rightarrow 0_1^+$  2229.7 keV transition, are given in the last column.

$E_\gamma^{\text{exp}}$ (keV)	$\gamma$ -ray transition	$E_\gamma$ (keV)	$I_\gamma$ (%)
1548.2	$0_2^+ \rightarrow 2_1^+$	3778.3	0.61(0.1)
1614.3	$4_1^- \rightarrow 3_1^-$	6621.1	3.48(0.6)
1755.5	$5_1^- \rightarrow 3_1^-$	6761.7	11.2(1.0)
1969.9	$^{36}\text{Ar}$	1970.4	
2161.3	$4_1^- \rightarrow 4_1^+$	6621.1	2.49(0.5)
2229.7	$2_1^+ \rightarrow 0_1^+$	2230.3	100(1.0)
2229.7	$4_1^+ \rightarrow 2_1^+$	4458.9	100(1.0)
2303.1	$5_1^- \rightarrow 4_1^+$	6761.7	1.06(0.2)
2392.5	$4_3^+ \rightarrow 4_1^+$	6852.0	1.57(0.5)
2569.7	$4_2^+ \rightarrow 2_2^+$	6411.0	3.96(0.6)
2701.2	$7_1^- \rightarrow 5_1^+$	9463.7	5.05(0.7)
2774.8	$3_1^- \rightarrow 2_1^+$	5006.2	18.2(1.4)
2944.9	$4_2^- \rightarrow 3_1^-$	7950.0	0.58(0.1)
3107.3	$5_1^+ \rightarrow 4_1^+$	7567.0	0.72(0.3)
3182.3	$3_1^+ \rightarrow 2_1^+$	5413.0	3.55(0.6)
3319.1	$2_3^+ \rightarrow 2_1^+$	5548.9	0.65(0.4)
3886.1	$6_1^+ \rightarrow 4_1^+$	8346.0	2,29(0.5)
3994.4	$2_1^- \rightarrow 2_1^+$	6224.3	0.85(0.4)
4180.7	$4_2^+ \rightarrow 2_1^+$	6411.0	1.26(0.5)
4282.2	$2_2^+ \rightarrow 0_1^+$	4281.5	6.93(1.5)
4693.0	$1_1^+ \rightarrow 0_1^+$	4695.4	0.85(0.3)
4776.5	$1_1^- \rightarrow 4_1^+$	9236.1	1.12(0.4)
5002.4	$3_1^- \rightarrow 0_1^+$	5006.2	0.72(0.3)
5323.2	$6_2^+ \rightarrow 4_1^+$	9783.5	1.71(0.4)
5796.8	$1_1^- \rightarrow 0_1^+$	5797.9	1.30(0.5)
6245.1	$1_3^- \rightarrow 2_1^+$	8494.0	?
6245.1	$0_3^+ \rightarrow 2_1^+$	6245.0	?
7429.3	$1_2^- \rightarrow 0_1^+$	7434.0	1.91(0.5)

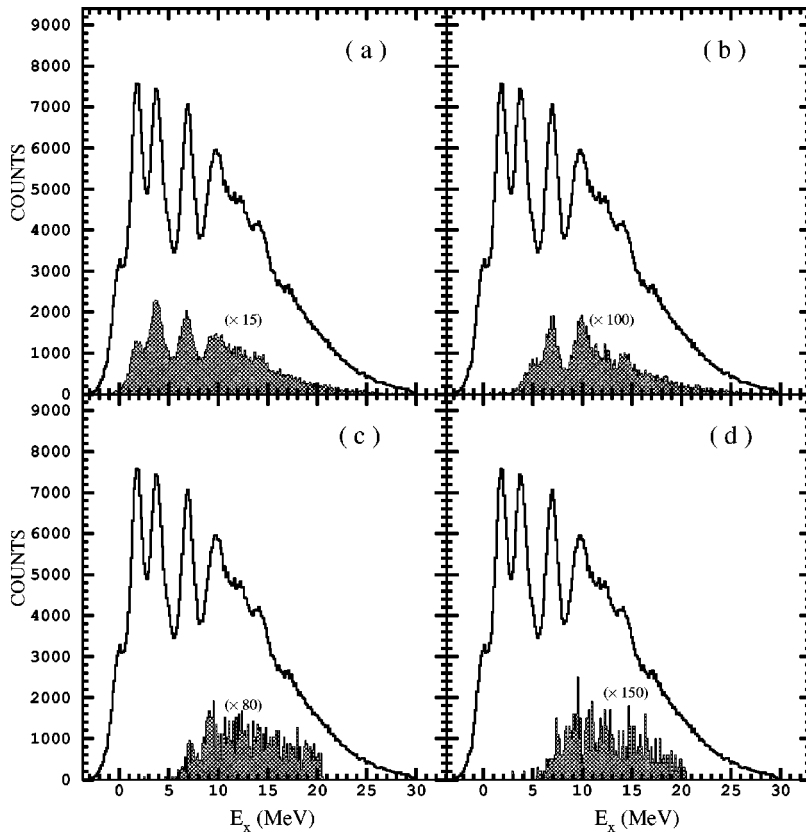


FIG. 12. Excitation-energy spectra of the  $^{28}\text{Si}+^{28}\text{Si}$  exit channel measured with no  $\gamma$ -ray condition (histograms) and as gated by the following  $\gamma$ -ray transitions in  $^{28}\text{Si}$  (shaded histograms): (a)  $2_1^+ \rightarrow 0_1^+$  ( $E_\gamma = 1778.9$  keV), (b)  $4_1^+ \rightarrow 2_1^+$  ( $E_\gamma = 2838.5$  keV), (c)  $4_2^+ \rightarrow 2_1^+$  ( $E_\gamma = 5110.0$  keV), and (d)  $3_1^- \rightarrow 0_1^+$  ( $E_\gamma = 6879.6$  keV).

two rotational bands  $K^\pi = 0^+$  [ $2_1^+$  (1368.7 keV),  $4_1^+$  (4122.9 keV),  $6_1^+$  (8113.4 keV)] and  $K^\pi = 2^+$  [ $2_2^+$  (4236.4 keV),  $3_1^+$  (5235.2 keV),  $4_2^+$  (6010.3 keV),  $6_2^+$  (9528 keV)], which are associated with stable prolate deformations, according to shell model calculations [74]. A selective population of natural-parity states has been found to be favored in the  $^{24}\text{Mg}+^{12}\text{C}$  orbiting reaction [75], with a suppression of the  $3_1^+$  (5235.2 keV) and  $5_1^+$  (7812.2 keV) states of the  $K=2$  band of  $^{24}\text{Mg}$ . In the  $^{32}\text{S}+^{24}\text{Mg}$  channel, the  $3^+$  state is populated rather strongly. The  $5^+$  state, however, is not seen. On the other hand, decays from even higher-energy  $6_1^+$  (8113.4 keV) and  $6_2^+$  (9528 keV) levels from  $K^\pi = 0^+$  and  $K^\pi = 2^+$  bands, respectively, are visible in the spectrum.

An interesting result for the  $^{32}\text{S}+^{24}\text{Mg}$  exit channel is found from inspection of the  $^{32}\text{S}$  gated spectrum of Fig. 9 (see Table IV) with the possible observation of previous unidentified  $\gamma$ -ray transitions in the  $^{32}\text{S}$  nucleus. Since both spherical and prolate band structures coexist, the  $^{32}\text{S}$  spectrum is much more complex than the  $^{24}\text{Mg}$  one. The spectroscopy of the  $^{32}\text{S}$  nucleus is of special interest; with the interplay between collective and single-particle motion at high spins at high excitation energy, superdeformed shapes may occur due to  $\alpha$  clusterization [65]. Recently, considerable effort has been devoted to the study of high-spin states in  $^{32}\text{S}$  both experimentally [66,67] and theoretically [68–71]. Thus, the  $\gamma$  rays associated with the  $^{32}\text{S}$  fragment, reported in Table IV, have been established with the aid of previous comprehensive spectroscopic studies [66,67]. Most of the high-energy states deexcite through one of the three most intense transitions  $2_1^+ \rightarrow 0_1^+$  (2230.3 keV),  $3_1^- \rightarrow 2_1^+$  (2776.0

keV), and  $3_1^+ \rightarrow 2_1^+$  (3183.0 keV). This has been checked by the inspection of the  $^{32}\text{S}+^{24}\text{Mg}$  excitation-energy spectrum of Fig. 4 when gated by one of these  $\gamma$  rays. In contrast to  $^{24}\text{Mg}$ , a large number of the most intense  $\gamma$  rays listed in Table IV involve high-spin negative-parity states such as  $3_1^-$  (5006.3 keV),  $4_1^-$  (6621.1 keV), and  $5_1^-$  (6761.7 keV). The respective measured feedings indicate that, according to their known branching ratios [63,68], the  $3_1^-$  state is, indeed, indirectly populated. The appearance of low-spin negative-parity states such as  $1_1^-$  (4693.0 keV),  $2_1^-$  (6224.3 keV), and, possibly  $1_3^-$  (8484.2 keV) may reflect an  $\alpha$ -transfer component to the reaction. This is consistent with the predictions of  $^{28}\text{Si} + \alpha$  cluster configurations for the low-lying bands of  $^{32}\text{S}$  [69]. On the other hand, why the positive parity states are not as strongly populated is not yet understood. The 8507.8 keV  $\gamma$ -ray transition is difficult to assign. However according to the branching ratios of the  $1_3^- \rightarrow 2_1^+$  (38%) arising from the  $^{32}\text{S}$  deexcitation [52], and despite the very low statistics, there is an indication in our data for the following new  $\gamma$ -ray transition  $0^+$  (8507.8 keV)  $\rightarrow$   $2_1^+$  (2230.2 keV).

### B. Coincident excitation-energy spectra

The large number of possible mutual excitations at the energies corresponding to the high-excitation structures (above  $E_x \approx 6.5$  MeV) apparent in Figs. 4 and 5 makes it impossible to uniquely identify those responsible for the data. However, the  $\gamma$ -ray data can be used to identify the dominant components of these structures, as shown by several examples presented in Figs. 12 and 13. The particle

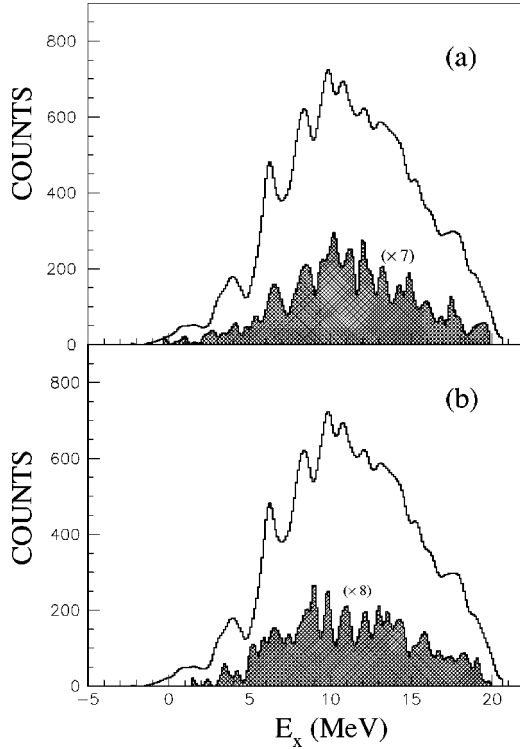


FIG. 13. Excitation-energy spectra of the  $^{32}\text{S}+^{24}\text{Mg}$  exit channel measured with no  $\gamma$ -ray condition (histograms) and as gated by the following  $\gamma$ -ray transitions (shaded histograms) :  $2_1^+ \rightarrow 0_1^+$  ( $E_\gamma = 1368.7$  keV) in  $^{24}\text{Mg}$  (a) and  $2_1^+ \rightarrow 0_1^+$  ( $E_\gamma = 2230.3$  keV) in  $^{32}\text{S}$  (b), respectively.

excitation-energy spectra of Figs. 12(a), 12(b), 12(c), and 12(e) have been obtained by gating on the  $2_1^+ \rightarrow 0_1^+$ ,  $4_1^+ \rightarrow 2_1^+$ ,  $4_2^+ \rightarrow 2_1^+$ , and  $3_1^- \rightarrow 0_1^+$ , transitions in  $^{28}\text{Si}$ , respectively. We have been able to construct other coincident spectra (not shown) obtained with gates on the weaker  $3_1^+ \rightarrow 2_1^+$ , and  $3_1^+ \rightarrow 0_1^+$   $\gamma$ -ray transitions (see Table II). They indicate significant contributions from the  $K^\pi = 3_1^+$  band.

It is evident that the populations by the selected mutual excitations are dominant. Contributions from a single excitation, such as the  $4^+$  state at 4617 keV, which appears as a small shoulder on the  $(2_1^+, 2_1^+)$  peak of the inclusive spectrum of Fig. 3, and which has been identified in previous works [9,31], appears more clearly in Figs. 12(b) when requiring a 2759 keV  $4_1^+ \rightarrow 2_1^+$  transition  $\gamma$  ray in coincidence. A detailed analysis of Fig. 12(b) shows that the main excitations which include the  $E_\gamma = 2838.5$  keV ( $4_1^+ \rightarrow 2_1^+$ )  $\gamma$ -ray transition in their decay chain are the  $(4_1^+, 0_1^+)$  single excitation state at  $E_X \approx 4.7$  MeV, the  $(4_1^+, 2_1^+)$  mutual state at  $E_X \approx 6.4$  MeV, and the  $(4_1^+, 4_1^+)$  mutual state at  $E_X \approx 9.4$  MeV. The  $(4_1^+, 4_2^+)$  and  $(4_1^+, 3_1^-)$  mutual excited states may correspond to a small structure lying near  $E_X \approx 12.0$  MeV. The  $(4_1^+, 6_1^+)$  mutual state which is centered at  $E_X \approx 14.0$  MeV is also clearly visible.

Figure 12(c) is associated with the  $E_\gamma = 5109$  keV ( $4_2^+ \rightarrow 2_1^+$ )  $\gamma$ -ray transition and contains a small peak at  $E_X \approx 6.9$  MeV (single excitation), and more intense peaks at  $E_X \approx 8.5$  MeV and 11.5 MeV corresponding to mutual exci-

tation states  $(4_2^+, 2_1^+)$  and  $(4_2^+, 4_1^+)$ , respectively. Although the statistics of Fig. 12(d) is very low, in the spectrum gated by the  $E_\gamma = 6879$  keV ( $3_1^- \rightarrow 0_1^+$ )  $\gamma$ -ray transition, the yield at  $E_X \approx 8.8$  MeV might arise from the  $(3_1^-, 2_1^+)$  mutual excited state, with the single excitation  $(3_1^-, 0_1^+)$  probability being almost nonexistent.

Figure 13 displays the coincident energy spectra gated by the indicated  $\gamma$ -ray transition in the  $^{24}\text{Mg}$  and  $^{32}\text{S}$  nuclei, respectively. For instance, the spectrum of Fig. 13(a) requires the observation of the  $2_1^+ \rightarrow 0_1^+$  transition in  $^{24}\text{Mg}$ . Narrow peaks are observed, some of which have high excitation energies and could not be reliably identified. The single excitation state [ $^{24}\text{Mg}(2_1^+)$ ,  $^{32}\text{S}(\text{g.s.})$ ] is weakly populated. In each case the data suggest a preferential population of high-spin mutual excitations.

To summarize, it can be concluded that the states of mutual excitation are favored. This is in contrast with the preferential population of single excitation states as usually observed for heavier nuclear systems in DI processes [24].

### C. Coincident $\gamma$ -ray angular correlations

The spin alignment of the low-lying excited states [single inelastic  $2_1^+$  and mutual inelastic  $(2_1^+, 2_1^+)$  exit channels] have been deduced based on particle-particle- $\gamma$  angular correlations using EUROGAM. This involves both  $^{28}\text{Si}$  fragments being detected in the  $\theta_{\text{c.m.}}^{\text{FF}} = 90^\circ \pm 7^\circ$  angular range (see Fig. 6), with very narrow coincident gates set either on the  $2_1^+$  peak or on the  $(2_1^+, 2_1^+)$  peak of Fig. 3. Three quantization axes are defined as (a) the beam axis, (b) the axis normal to the scattering plane, and (c) the axis perpendicular to both axes defined in (a) and (b). Since the two  $^{28}\text{Si}$  fragments are detected in the angular region near  $\theta_{\text{c.m.}}^{\text{FF}} = 90^\circ$ , the (c) axis corresponds approximately to the molecular axis of the outgoing binary fragments. In Figs. 14 and 15 the results of the  $\gamma$ -ray angular correlations for the single excitation and for the mutual excitation exit channels are shown. The distributions are presented in terms of the polar angles with respect to the three different quantization axes. The analysis method of the  $W(\theta_\gamma)$  data is described in Ref. [47], in which the process of integration over  $\phi_\gamma$  requires, due to the geometry of the EUROGAM spectrometer, some averaging over  $\theta_\gamma$ . Our experimental efficiency for particle-particle- $\gamma$ - $\gamma$  detection is low and, consequently, the analysis was done with the condition of a  $\gamma$  multiplicity equal to 1. For the mutual excitation exit channel, the strong minimum in Fig. 15(b) at  $90^\circ$  implies that the magnetic substate  $m$  is equal to zero ( $m=0$ ), and, thus, that the intrinsic spin vectors of the  $2^+$  states are oriented in the reaction plane perpendicularly to the orbital angular momentum. The value of the total angular momentum, therefore, remains close to  $L=38\hbar$ , in good agreement with the angular distributions results. The  $4\pi$  geometry of the  $\gamma$ -ray spectrometer also allowed us to fit the  $W(\theta_\gamma)$  (see the solid curves in Figs. 14 and 15) to obtain more quantitative information about the contributions from the different magnetic substates. As proposed in Ref. [17], the  $W(\theta_\gamma)$  data have been described by an expression of the form  $W(\theta_\gamma) = \sum_m P_m W_m(\theta_\gamma)$ , where the  $P_m$  coefficients rep-

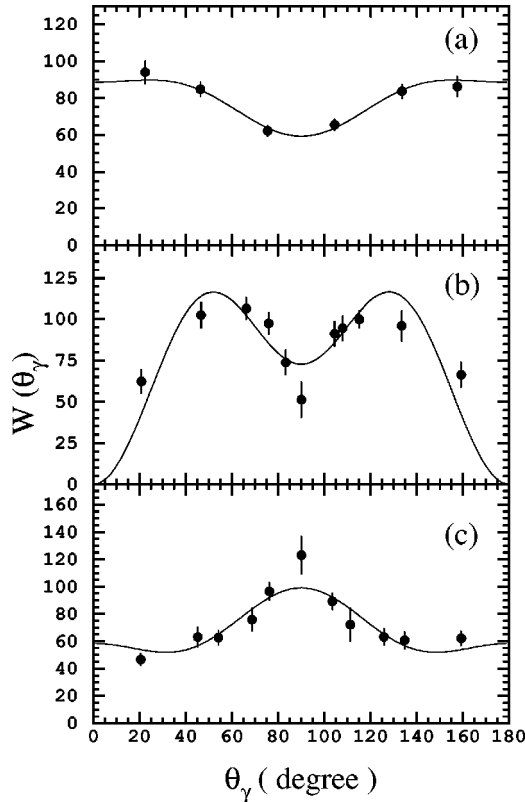


FIG. 14.  $\gamma$ -ray angular correlations for the  $(2_1^+, 0_1^+)$  state of the  $^{28}\text{Si}+^{28}\text{Si}$  exit-channel for the three different quantization axes defined in the text. The solid curves are fits of the data.

resent either the magnetic substate population parameters in single or mutual  $2^+$  inelastic scattering, or the relative intensities of transitions with different  $\Delta m$  for  $E2$  transitions between higher excited states. Since the parameters  $P_m$  enter the expression as linear coefficients of the pure- $\Delta m$  functions  $W_{\Delta m}(\theta_\gamma)$ , the fits were calculated using a simple linear least squares procedure [17]. The fit produces [47] a significant  $m=0$  substate population, favored for both quantization axes (a) and (b) but not for (c). The characteristic “ $m=0$ ” pattern, observed in Fig. 15(b) suggests that the fragment spins  $\mathbf{I}_1$  and  $\mathbf{I}_2$  are indeed oriented in the reaction plane perpendicularly to the total angular momentum. The non-negligible  $m=\pm 2$  contributions (see Table I of Ref. [47]) are consistent with the analysis of the angular distribution which contains contributions from  $L=36\hbar$  and  $L=40\hbar$ . Admixtures of these other smaller contributions do not affect the observation of the dominant “disalignment” component consistent with the results of the angular distributions. Such lack of alignments of the fragment spins are unusual in DI processes [24], but the very long lifetime of the resonance may well allow large microscopic fluctuations.

## V. DISCUSSION

Before any attempt is made to understand the occurrence of a strong resonance component for the low-energy states, the observation of relatively narrow structures (less than 1.5 MeV) in the excitation energy spectra above  $E_X=10$  MeV

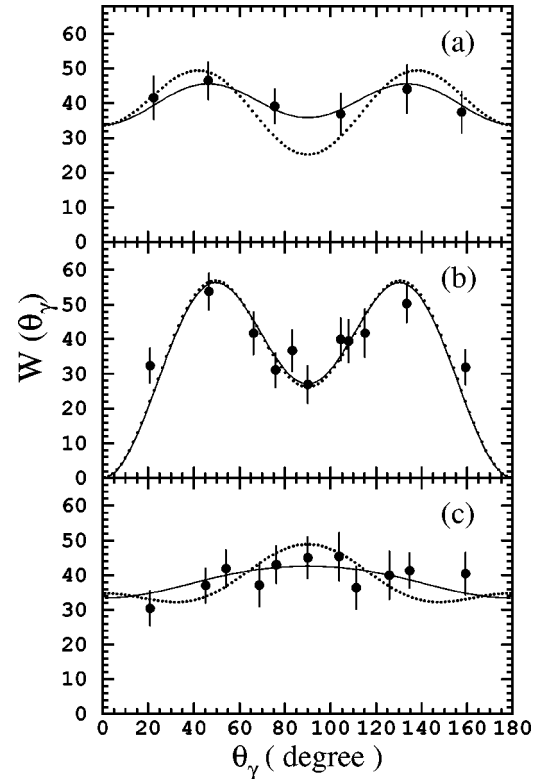


FIG. 15.  $\gamma$ -ray angular correlations of the  $(2_1^+, 2_1^+)$  state of the  $^{28}\text{Si}+^{28}\text{Si}$  exit-channel for the three quantization axes defined in the text. The solid and dashed curves are fits of the data and molecular-model predictions, respectively.

needs to be clarified since one might be tempted to attribute these structures to a mechanism other than FF as well. In the following discussion, we first give a comparison of the measured excitation-energy spectra and of the feedings of their associated states with TSM calculations. A comparison of the resonances seen in different nuclear systems is discussed along with a dynamical description of the resonant behavior proposed for both  $^{28}\text{Si}+^{28}\text{Si}$  and  $^{24}\text{Mg}+^{24}\text{Mg}$  in the framework of a newly developed molecular model [42–44]. Alternative theoretical approaches of the  $^{28}\text{Si}+^{28}\text{Si}$  resonances are also briefly presented.

### A. TSM calculations

A quantitative description of the FF process in light systems has been developed in terms of the transition-state model [33]. In TSM, where fission competes with  $\gamma$ -ray and light-particle emission in the CN deexcitation, the probability for fission is determined by the most restrictive phase space (level density) encountered by the fissioning system between the equilibrated CN configuration and the exit channel. This “transition state” is usually taken as the configuration at the saddle point where the macroscopic potential energy surface reaches its maximum value.

Calculation of fission cross sections in the statistical model is based on the Hauser-Feshbach formalism [24]. For a CN of spin  $J$ , populated with a partial fusion cross section of  $\sigma_J$ , the partial fission cross section is given in terms of the

ratio of the fission decay width  $\Gamma_J^{\text{fis}}$  to the total decay width for this spin  $\Gamma_J^{\text{tot}}$ , by

$$\sigma_J^{\text{fis}} = \frac{\Gamma_J^{\text{fis}}}{\Gamma_J^{\text{tot}}} \sigma_J. \quad (2)$$

The fusion partial cross section for formation of a CN of spin  $J$  from projectile and target nuclei of spins  $J_p$  and  $J_t$ , respectively, at a center-of-mass energy  $E_{\text{c.m.}}$  is given by

$$\sigma_J = \pi \chi^2 \frac{2J+1}{(2J_p+1)(2J_t+1)} \sum_{S=|J_p-J_t|}^{J_p+J_t} \sum_{l=|J-S|}^{J+S} T_l(E_{\text{c.m.}}) \quad (3)$$

with

$$\sigma_{\text{fus}}^{\text{tot}} = \sum_{J=0}^{\infty} \sigma_J. \quad (4)$$

A simple and commonly used method of representing the fusion transmission coefficient is to take

$$T_l(E_{\text{c.m.}}) = \frac{1}{1 + \exp\{[l - l_{\text{cr}}(E_{\text{c.m.}})]/\Delta\}}, \quad (5)$$

where  $l_{\text{cr}}$  is the critical angular momentum for fusion and  $\Delta$  is the diffuseness of the fusion  $l$  distribution. The critical angular momentum for fusion  $l_{\text{cr}}$  can either be obtained from fusion model calculations [33] or by adjusting its value to achieve consistency with measured ER cross sections [34]. Most of the calculations for the lighter systems have been performed by using a rather sharp value  $\Delta = 1\hbar$  for the diffuseness parameter.

For the calculation of the total decay width  $\Gamma_{\text{tot}}$ , it is assumed that the CN deexcitation occurs through the emission of neutrons, protons,  $\alpha$  particles,  $\gamma$  rays, and/or fission fragments. Under these conditions, the total width  $\Gamma_{\text{tot}}$  can be written as

$$\Gamma_{\text{tot}} = \Gamma_n + \Gamma_p + \Gamma_\alpha + \Gamma_\gamma + \Gamma_{\text{fis}}. \quad (6)$$

Here, the partial width  $\Gamma_x$  for particle  $x$  ( $x=n, p$ , or  $\alpha$ ) of spin  $s_x$  to be emitted from the CN with excitation energy  $E_{\text{CN}}^*$  and spin  $J_{\text{CN}}$  to form an evaporation-residue nucleus ER of excitation energy  $E_{\text{ER}}^*$  and spin  $J_{\text{ER}}$  is given by

$$\Gamma_x = \int \frac{\rho_{\text{ER}}(E_{\text{ER}}^* - \Delta_{\text{eff}}, J_{\text{ER}})}{2\pi\rho_{\text{CN}}(E_{\text{CN}}^* - \Delta_{\text{eff}}, J_{\text{CN}})} \times \sum_{S=|J_{\text{ER}}-s_x|}^{J_{\text{ER}}+s_x} \sum_{l=|J_{\text{CN}}-S|}^{J_{\text{CN}}+S} T_l^x(\varepsilon_x) d\varepsilon_x. \quad (7)$$

The integral is over all kinetic energies of the emitted light particle  $\varepsilon_x$ , and  $\rho_{\text{CN}}$  and  $\rho_{\text{ER}}$  are the level densities of the CN and resulting ER, respectively. The parameter  $\Delta_{\text{eff}}$  determines the zero point of the effective excitation energy, with

$$\Delta_{\text{eff}}(\text{MeV}) = E_B(Z, A) - E_B^{\text{macro}}(Z, A). \quad (8)$$

Here  $E_B$  is the measured binding energy of the nucleus and  $E_B^{\text{macro}}$  is the corresponding macroscopic energy [31]. For ER's the transmission probabilities  $T_l^x(\varepsilon_x)$  are obtained from optical-model calculations with average parameters. For FF the transmission coefficients are taken as unity for energetically allowed paths and zero, otherwise.

To calculate the level densities of the CN and the saddle-point configurations, a Fermi-gas formula [31,33,36] is used. For ER, the level-density parameter  $a_x = a_n$ . The saddle-point densities are calculated with  $a_x = a_f$  and  $J = J_{\text{CN}}$ . Most of the calculations done for light systems have used  $a_n = A_{\text{ER}}/8$  and  $a_f = A_{\text{CN}}/8$ .

In light nuclear systems, the fission breakup of the CN occurs often to final fragments where the density of states is low. This can result in considerable structure in the excitation spectra of the fission fragments. To explore the population of states in the final fragments while retaining the saddle-point as the ‘‘transition’’ state, a procedure has been developed [31] to calculate the population of specific mutual excitations assuming a stochastic process. Within the transition-state method, population of a given saddle-point level already corresponds to a commitment to fission into a particular mass partition. The partial cross section for the population of the CN with spin  $J$  that subsequently undergoes fission to mass asymmetry  $\eta$  is taken as  $\sigma_{\text{FF}}(J, \eta)$  and is calculated using TSM based on the saddle-point phase space. The cross section for populating a specific mutual excitation  $(\beta_1, \beta_2)$  is then given by

$$\sigma(\beta_1, \beta_2) = \sum_J \sigma_{\text{FF}}(J, \eta) \frac{\sum_{l_{\text{out}}} [\beta_1 \times \beta_2]_{J, l_{\text{out}}} P(\eta, J, \varepsilon)}{\sum_{\lambda_1, \lambda_2, l_{\text{out}}} [\lambda_1 \times \lambda_2]_{J, l_{\text{out}}} P(\eta, J, \varepsilon)}, \quad (9)$$

where  $[\lambda_1 \times \lambda_2]_{J, l_{\text{out}}}$  represents the sum of the possible spin couplings between the two fragments in states  $\lambda_1$  and  $\lambda_2$  with orbital angular momentum  $l_{\text{out}}$  and coupling to CN spin  $J$ , and  $P(\eta, J, \varepsilon)$  is the probability of the CN of spin  $J$  to fission with mass asymmetry  $\eta$  and radial kinetic energy  $\varepsilon$ . This probability depends implicitly on  $l_{\text{out}}$  through  $\varepsilon$ .

The radial kinetic energy  $\varepsilon$  can be expressed in terms of the characteristic energies of the reaction with

$$\varepsilon = E_{\text{c.m.}} + Q_0 - V_{\text{rel}}(l_{\text{out}}, \eta) + \delta - E_x. \quad (10)$$

Here,  $E_{\text{c.m.}}$  is the center-of-mass energy in the entrance channel,  $Q_0$  is the ground-state  $Q$  value,  $V_{\text{rel}}(l_{\text{out}}, \eta)$  is the relative energy of the two spheroids that comprise the saddle-point shape,  $\delta$  is the energy loss that occurs in moving from the saddle to scission configurations, and  $E_x$  is the mutual excitation of the final fragments. In light systems  $\delta$  is expected to be small, and a value of  $\delta = 2.5$  MeV was used in all the calculations to be consistent with the saddle and scission configurations being similar. The parameters used to determine partial cross sections to specific mutual excitations were the same as those discussed in Ref. [31]. The  $l_{\text{cr}}$  value was obtained so as to reproduce the measured CF cross sec-

tion [57,59] (the adopted  $l_{cr}=35\hbar$  value assumes a total fusion cross section of 1160 mb, leading to a calculated ER cross section of 1028 mb at 111.6 MeV, to be compared with the experimental value of  $1003\pm 25$  mb measured by Di-Cenzo *et al.* [57] at 110 MeV). The spin weighting was determined by the level schemes for the  $^{24}\text{Mg}$ ,  $^{28}\text{Si}$ , and  $^{32}\text{S}$  fragments known from compilations found in the literature [31,36,60–64,66]. Further details of the calculations can be found in Ref. [31].

Figures 4 and 5 compare the results of this calculation with the observed excitation spectra for both the  $^{28}\text{Si}(^{28}\text{Si}, ^{28}\text{Si})^{28}\text{Si}$  and  $^{28}\text{Si}(^{28}\text{Si}, ^{32}\text{S})^{24}\text{Mg}$  reaction channels. The bold-line histograms represent the experimental results. The solid line of Fig. 3 shows the predicted spectra using all known levels in  $^{28}\text{Si}$  up to the 14.339 MeV excitation. The dotted line is the predicted spectrum for only the particle-bound levels. Since the experimental results were obtained using a kinematic coincidence technique that discriminates against excitations where one or both of the populated states subsequently emits a light particle, the thin-line histograms are expected to more faithfully represent the experimental situation. The calculated spectra for particle-bound states are found to reproduce the observed structures quite well, in particular in the  $E_X\approx 9\text{--}17$  MeV region. The structure observed at higher excitation energies ( $10\leq E_X\leq 15$  MeV) can be attributed to groupings of mutual excitations with high channel spins. The calculations are less successful in reproducing the yields at yet higher energies ( $E_X\geq 15$  MeV) for the two channels, possibly because of the incomplete knowledge about states at high excitation energy in the fragments. The observed structure in the low-energy region is very badly reproduced by the calculations, which significantly underestimate the cross section for the low-lying states excited in the  $^{28}\text{Si}+^{28}\text{Si}$  exit channel. This result is consistent with the states being dominated by another reaction process: the heavy-ion resonance behavior.

The essential validity of the predicted population pattern was confirmed by the measurements of the  $\gamma$  rays in coincidence with the fission fragments. Figure 10 shows the comparison between the experimental feedings (diamonds and triangles) for states in  $^{28}\text{Si}$  populated in the ‘‘large-angle region’’ and the theoretical feedings (histograms) predicted by the TSM. The feedings for states populated in  $^{24}\text{Mg}$  and  $^{32}\text{S}$  were not compared to the TSM predictions first because of their rather low statistics and, secondly, because of the  $4_1^+\rightarrow 2_1^+$  and  $2_1^+\rightarrow 0^+$  transitions have almost the same  $\gamma$ -ray energy. We can remark that the TSM does not reproduce the experimental data on the feeding of the  $0_1^+(K^\pi=0_1^+)$ ,  $2_1^+(K^\pi=0_1^+)$ ,  $4_3^+(K^\pi=0_3^+)$  and  $4_1^-(K^\pi=3_1^-)$  states of  $^{28}\text{Si}$  well. The disagreement between experimental data and model calculations for the feeding of the  $0_1^+$  and  $2_1^+$  states of the  $^{28}\text{Si}$  ground band is expected to be due to resonant effects. The strong population of the highly deformed prolate band  $K^\pi=0_3^+$  in the ‘‘large-angle region’’ confirms what has been previously observed in the  $^{32}\text{S}+^{24}\text{Mg}$  reaction [31]. A satisfactory explanation for the disagreement for the feeding of the  $4_3^+(K^\pi=0_3^+)$  and  $4_1^-(K^\pi=3_1^-)$  states is more difficult to provide as it may reflect aspects of the

nuclear structure that cannot be described by the statistical picture. In the following subsections, the excess of resonant yields for the low-lying states, which could not be explained in terms of a statistical process by the TSM, will be considered as due to resonant effects, and tentatively discussed in the framework of resonance models.

## B. Comparison with different nuclear systems

For a general understanding of the resonant behavior in heavy-ion scattering, it is of interest to compare the resonances observed for medium-mass systems, such as the  $^{28}\text{Si}+^{28}\text{Si}$  [7–12] and the  $^{24}\text{Mg}+^{24}\text{Mg}$  [13–17] systems, with those occurring in a lighter system such as  $^{12}\text{C}+^{12}\text{C}$  [1,4,5,76]. The broad structures in the  $^{28}\text{Si}+^{28}\text{Si}$  and the  $^{24}\text{Mg}+^{24}\text{Mg}$  excitation functions are essentially the same as those reported for the  $^{12}\text{C}+^{12}\text{C}$  system at energies well above the Coulomb barrier [1,5,76]. While the narrow structure seems confined to one region of energy in the  $^{28}\text{Si}+^{28}\text{Si}$  ( $E_{\text{lab}}=100\text{--}130$  MeV) and  $^{24}\text{Mg}+^{24}\text{Mg}$  ( $E_{\text{lab}}=70\text{--}100$  MeV) systems, it is much more widely spread in the  $^{12}\text{C}+^{12}\text{C}$  system. A common feature, however, seems to be the disappearance of the narrow structures at the highest energies where strong absorption effects are expected based on NOC [21,22] calculations. In all cases the sequence of spins follows closely that of the grazing partial wave and, thus,  $^{28}\text{Si}+^{28}\text{Si}$  does not seem to be appreciably different from  $^{12}\text{C}+^{12}\text{C}$ . However, there are significant differences in the pattern of their respective resonance widths. For example, the partial width for decay into the  $^{28}\text{Si}+^{28}\text{Si}$  elastic channel is typically only of the order of 1% of the total resonance width, as found in the literature [6]. This is considerably smaller than the corresponding partial width for decay into the  $^{12}\text{C}+^{12}\text{C}$  elastic channel, which is a large fraction of the total resonance width (15–30%). In general, for the lightest systems, the total width of the resonances can be accounted for in experimentally measured channels, whereas for the heavier systems only approximately one third of the total width is observed in binary reaction channels. In this case the width of decay to excited states plays a much more significant role in the  $^{28}\text{Si}+^{28}\text{Si}$  system than in a lighter one such as  $^{12}\text{C}+^{12}\text{C}$ . The most surprising difference is the apparent complexity of the inelastic decay channels in the  $^{28}\text{Si}+^{28}\text{Si}$  case.

The observation of spin alignment was first made for the  $^{12}\text{C}+^{12}\text{C}$  molecular resonances by a group in Munich [76]. In this case the correlation between the spin orientations of the two  $^{12}\text{C}$  nuclei in mutual inelastic scattering was deduced from the directional correlations of the particle-coincident  $\gamma$ -ray measured with the Darmstadt-Heidelberg crystal ball detector. The resonant behavior in the excitation functions was found to be nearly uniquely associated with the mutually aligned component. The series of strong  $^{12}\text{C}+^{12}\text{C}$  resonances [1,5] (both the correlated gross and intermediate-width structures in the excitation functions) were systematically reproduced quite well by the band crossing model [77] (BCM). Similar results are observed in other systems such as the  $^{12}\text{C}+^{16}\text{O}$  and  $^{16}\text{O}+^{16}\text{O}$  systems. In the BCM [77], it is assumed that only a few channel components with aligned

spin coupling contribute significantly to the feeding of the resonant states. This is consistent with the partial widths and spin alignments, as measured in the inelastic channels [76]. Although some aspects still remain to be fully understood, the characteristic points are that about one half or more of the total width is exhausted by the partial widths to a few relevant channels and that the spin alignments are enhanced.

Shortly after the first observation of the spin alignment in the  $^{12}\text{C} + ^{12}\text{C}$  molecular resonances [76], Wuosmaa *et al.* [15,17] measured the single and correlated magnetic-substate population parameters for the  $2_1^+$  and  $2^+ - 2^+$  excitations in the prolate-prolate  $^{24}\text{Mg} + ^{24}\text{Mg}$  system. These measurements were performed in the region of two strong resonances observed at  $E_{\text{c.m.}} = 45.70$  and  $46.65$  MeV in the inelastic scattering data. Both the  $\gamma$ -ray angular correlation and the angular distribution measurements were performed using the Oak Ridge Spin Spectrometer. A similar experiment was also carried out by the Munich group [16]. Both sets of data have provided spectroscopic information relatively free from nonresonant amplitudes, and allow a spin assignment of  $J^\pi = 36^+$  for at least the first of the two resonances. The angular correlation data for the mutual  $2^+$  inelastic scattering channel suggested a dominant angular momentum value of  $L = 34\hbar$  for both resonances. The spin alignment data for this channel confirm the partial alignment of the fragment spins with the orbital angular momentum. The relatively high spin values suggest a resonance configuration in which the two  $^{24}\text{Mg}$  nuclei interact in a pole-to-pole configuration, allowing the system to sustain a large amount of angular momentum. This hypothesis was corroborated by a molecular model [42] which is described in the following subsection.

The present  $^{28}\text{Si} + ^{28}\text{Si}$  data show, for the first time in a heavy-ion collision, a vanishing spin alignment. Therefore, the comparison between the three symmetric systems  $^{12}\text{C} + ^{12}\text{C}$ ,  $^{24}\text{Mg} + ^{24}\text{Mg}$ , and  $^{28}\text{Si} + ^{28}\text{Si}$  shows an interesting contrast in the spin orientation at resonance energies. The results indicate that the  $^{28}\text{Si} + ^{28}\text{Si}$  oblate-oblate system is characterized by spin disalignment in contrast to the spin alignment observed for both the  $^{12}\text{C} + ^{12}\text{C}$  system (oblate-oblate) and the  $^{24}\text{Mg} + ^{24}\text{Mg}$  system (prolate-prolate). As will be shown in Sec. V C, molecular-model calculations are able to explain the vanishing spin alignment in the oblate-oblate  $^{28}\text{Si} + ^{28}\text{Si}$  system [47], where both nuclear spin vectors are perpendicular to the orbital angular momentum lying in the reaction plane. The question of why the spin orientations in the two oblate-oblate systems  $^{28}\text{Si} + ^{28}\text{Si}$  and  $^{12}\text{C} + ^{12}\text{C}$  are so different is still unclear. However, it can be also noted that the weak coupling picture of the BCM [77] appears to be adequate for the  $^{12}\text{C} + ^{12}\text{C}$  system while the strong coupling picture of the molecular model appears to reproduce the  $^{28}\text{Si} + ^{28}\text{Si}$  results better. Differences in the interactions between the constituent nuclei may play a key role. For example, there is a remarkable difference in the available molecular configurations in the excitation spectra of the  $^{12}\text{C}$  and  $^{28}\text{Si}$  nuclei. In  $^{12}\text{C} + ^{12}\text{C}$  there are few molecular configurations, located at the energies associated with the observed resonances, while in  $^{28}\text{Si} + ^{28}\text{Si}$  there are many

more configurations available as based on NOC calculations [21,22]. It is possible that the large number of available configurations allows for the formation of coherent or collective states. This explains the sharp resonances which decay into many inelastic channels. In the  $^{12}\text{C} + ^{12}\text{C}$  system, such coherent effects may not be allowed to develop. In this case the individual configurations may be observed. This situation corresponds well to the BCM calculations [77] which predict enhanced excitations of states where both nuclear spins and the orbital angular momentum are aligned perpendicularly to the scattering plane. Actually, the  $^{28}\text{Si} + ^{28}\text{Si}$  data as well as the  $^{24}\text{Mg} + ^{24}\text{Mg}$  data both show that the resonances are well correlated among many inelastic channels, suggesting that the interaction is effectively strong, and the resultant resonance states include many components (partial widths) over the available reaction channels. This is in contrast to the situation in the lighter  $^{12}\text{C} + ^{12}\text{C}$  system. Therefore, older resonance models such as the BCM [77] may not be adequate to describe the  $^{28}\text{Si} + ^{28}\text{Si}$  and  $^{24}\text{Mg} + ^{24}\text{Mg}$  systems accurately. A more appropriate description of these systems may be in terms of quasibound molecular states as predicted by the molecular model [42–44,78–80,82,83] This model is presented in the following section.

### C. Molecular model predictions

Although the present paper remains essentially an experimental study, it is of interest to briefly present the main ideas contained in the molecular model developed simultaneously by Uegaki and Abe [42–44] on the one hand and by Maass and Scheid [78–80] on the other hand. When two nuclei form a nuclear molecule by touching each other only in their surface zones, a rich variety of new collective modes of excitations, such as the so-called butterfly, the antibutterfly, and the belly-dancer types of motions, may appear [83]. In solving the equations of motion for these systems,  $\beta$  and  $\gamma$  vibrational degrees of freedom of the individual nuclei are also included in the calculations [2]. Although for light systems, the direct experimental investigation of these dynamical modes is a formidable task, such a model helps to understand how the complexity of the  $^{28}\text{Si} + ^{28}\text{Si}$  resonances [7–12] can be different from that of the  $^{24}\text{Mg} + ^{24}\text{Mg}$  resonances [13–17]. Most of the molecular model predictions have been devoted to the prolate-prolate  $^{24}\text{Mg} + ^{24}\text{Mg}$  system [42,43,78–80], and, more recently, to the oblate-to-oblate systems  $^{28}\text{Si} + ^{28}\text{Si}$  [44] and  $^{12}\text{C} + ^{12}\text{C}$  [82] systems. For the  $^{24}\text{Mg} + ^{24}\text{Mg}$  system both available versions of the molecular model consider various, but different excitation modes with respect to the favored equilibrium configuration. As a result, both models identify a number of quasibound molecular states with level densities, energies, and decay widths in qualitative agreement with the measured resonances. The most recent theoretical developments of the molecular model, as applied to the  $^{28}\text{Si} + ^{28}\text{Si}$  reaction, will be presented elsewhere by Uegaki and Abe [46]. However, preliminary calculations [35,47,53,56] of the  $^{28}\text{Si} + ^{28}\text{Si}$  scattering with the molecular model predict an oblate-oblate dinuclear system with an equator-to-equator stable configuration [44], whereas the resonancelike structure observed for  $^{24}\text{Mg}$

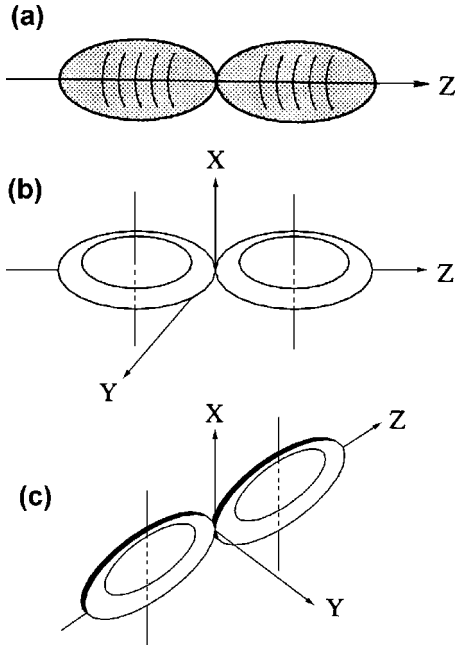


FIG. 16. Equilibrium configurations of three different dinuclear systems : (a) for  $^{24}\text{Mg}+^{24}\text{Mg}$ , (b) for  $^{28}\text{Si}+^{28}\text{Si}$ , and (c) for  $^{12}\text{C}+^{12}\text{C}$ .

$+^{24}\text{Mg}$  appears to be linked to a prolate-prolate dinuclear system [42] in a pole-pole configuration.

The general concept of the molecular model [42–44] is based on simple considerations that, at very high spins ( $L = 34\hbar - 46\hbar$ ), the dinuclear configurations tend to have very elongated, but stable shapes due to the dominant centrifugal forces. Three typical, equilibrium configurations are sketched in Fig. 16 for the  $^{24}\text{Mg}+^{24}\text{Mg}$ ,  $^{28}\text{Si}+^{28}\text{Si}$ , and  $^{12}\text{C}+^{12}\text{C}$  systems, respectively. The characteristic normal excitation modes of motion of these configurations may be responsible of the observed resonant structures. The stable configuration of prolate-prolate systems, such as  $^{24}\text{Mg}+^{24}\text{Mg}$ , is shown in Fig. 16(a) and is predicted to be a pole-to-pole configuration, as a consequence of the prolate shape of the interacting  $^{24}\text{Mg}$  nuclei. In the case of collisions between two oblate deformed nuclei, as is shown in Figs. 16(b) and 16(c), it has been speculated that an equator-equator touching configuration is favored [72]. The observed mismatch of the spin vectors in  $^{28}\text{Si}+^{28}\text{Si}$  with the orbital angular momentum have tentatively been discussed [35,53] as a candidate for a butterfly mode of excitation, where the intrinsic spins of the two interacting nuclei couple to zero.

The rotating molecular frame of the dinuclear system has been defined (see the schematical view of the Fig. 1 in Ref. [44]) to describe quantitatively the collective motions of the intrinsic states. For the sake of simplicity, the constituent nuclei such as  $^{24}\text{Mg}$  and  $^{28}\text{Si}$  are assumed to have a constant deformation and the axial symmetry. Still, the dynamical equations need to be solved with seven degrees of freedom [43]. Three degrees of freedom are from the relative vector  $R=(R, \theta_1, \theta_2)$ . The collective degrees of freedom of deformed nuclei are the orientations of the symmetry axes, which are described by the Euler angles  $(\alpha_1, \beta_1)$  and

$(\alpha_2, \beta_2)$ . The two angles  $\alpha_1$  and  $\alpha_2$  are combined into  $\theta_3 = (\alpha_1 + \alpha_2)/2$  and  $\alpha = (\alpha_1 - \alpha_2)/2$ . The generalized coordinates  $(q_i) = (\theta_1, \theta_2, \theta_3, R, \alpha, \beta_1, \beta_2)$ , have been defined with  $\theta_i$ 's being the Euler angles of the molecular frame with four internal variables. Consistent with the chosen coordinate system, a rotation-vibration type of wave function such as  $\Psi \sim D_{MK}^J(\theta_i)\chi_K(R, \alpha, \beta_1, \beta_2)$ , where  $\chi_K$  describes internal motions, has been introduced [44].

The dynamical equations of the internal motions have been solved around equilibrium, and various normal modes, butterfly and antibutterfly vibrational modes, as well as  $K$ -rotational (where  $K$  is the projection of the total angular momentum quantum number  $J$  onto the center axis of the two separated fragments [81] normally denoted as the nuclear symmetry  $z$  axis) and twisting-rotational modes have been obtained [44]. Each vibrational mode has its characteristic feature with respect to the alignments. For instance, in a butterfly mode of excitation, the interacting nuclei move coherently, therefore the intrinsic spin  $I=I_1+I_2=0$ , while in an antibutterfly mode, the spins are parallel so as to yield the total spin to be maximum. Molecular model calculations for spin distributions of the normal-mode motions were performed for the mutual inelastic channels for both the  $^{28}\text{Si}+^{28}\text{Si}$  and  $^{24}\text{Mg}+^{24}\text{Mg}$  reactions [35,45,53]. A concentration of the probabilities for channel spin of  $I=0$  for the butterfly motion was found for the  $^{28}\text{Si}+^{28}\text{Si}$  reaction. This is consistent with the angular distribution data shown in Fig. 6, with  $L=J$ . The present fragment-fragment- $\gamma$  coincidence data for the mutual excitation exit-channel, shown in Fig. 15 for the decay of the  $38^+$  resonance, indicate orientations for the fragments spins in the resonance state which are both in the reaction plane. To explain the experimental observations, the molecular model has been further developed [47] to include mixing of the  $K$  quantum number.

A rotating molecular frame is introduced, with the  $z$  axis parallel to the relative vector of the two interacting nuclei. Figure 16(b) illustrates the triaxial configuration of the oblate-oblate system which rotates around the  $z$  axis which is parallel to the normal of the reaction plane. The scenario is different for prolate-prolate cases such as  $^{24}\text{Mg}+^{24}\text{Mg}$  in Fig. 16(a), where the pole-pole configuration is axially symmetric. For the oblate-oblate system, the moments of inertia of the rigid dinucleus configuration is  $I_x = \mu R^2 + I_z^0 \times 2$ ,  $I_y = \mu R^2 + I_x^0 \times 2$ ,  $I_z = I_y^0 \times 2 = I_x^0 \times 2$ , where  $\mu$  is the reduced mass,  $R$  the relative distance joining the mass centres of two interacting nuclei, and  $I_i^0$  is the moment of inertia of the fragment around its intrinsic  $i$  axis, taking the symmetry axis as the intrinsic  $z$  axis. This means that  $K$  is not a good quantum number. The mixing of the  $K$  quantum number is calculated by diagonalization of the rotational energy, which is approximately equivalent to solving the harmonic oscillator in  $K$  space in the high spin limit (when  $K/J \approx 0$ ). The solution is a Gaussian function multiplied by an Hermite polynomial  $f_n(K) = H_n(K/b)\exp[-(K/b)^2/2]$  where the width parameter  $b$  is given by  $b = (2J^2 I_K / \Delta)^{1/4}$ , where  $I_K^{-1} = I_z^{-1} - I_{av}^{-1}$  and  $\Delta^{-1} = I_y^{-1} - I_{av}^{-1}$  with  $I_{av}^{-1} = \frac{1}{2}(I_x^{-1} + I_y^{-1})$ . Since the  $K$  mixing gives the distribution of orientations of the whole system around the molecular  $z$  axis, orientations of the

fragment spins (pancakes) have the same distribution. It is interesting to notice that, for large values of  $J$ ,  $K=0$  implies that the angular distributions of this rotating system approach the  $1/\sin(\theta)$  angular distribution expected classically for an isotropic emission. The angular correlation of a  $\gamma$  ray emitted from the fragments is calculated with this distribution of the spin orientation for  $b=1.3$  (a value which is consistent with the dinuclear configuration), and compared with the measurements in Fig. 15 for all the three axes (a), (b), and (c). The good agreement found for the mutual excitation exit channel is consistent with a strong concentration in “ $m=0$ ” states. Calculations for the single excitation exit channel are in progress [46].

The observation for the  $^{28}\text{Si}+^{28}\text{Si}$  (oblate-oblate) system of a vanishing spin alignment may result from a butterfly motion and tilting mode. On the other hand, the channel spin probabilities calculated for the  $^{24}\text{Mg}+^{24}\text{Mg}$  (prolate-prolate) system do not show such an  $I=0$  concentration as found for the butterfly mode of excitation, due to a fluctuation in the small probabilities. The results of the present analysis are encouraging for further investigations of fragment spin alignment associated with heavy-ion resonances. These measurements promise to develop important new structural information on the resonance states in  $^{24}\text{Mg}+^{24}\text{Mg}$  and  $^{28}\text{Si}+^{28}\text{Si}$ . The  $^{12}\text{C}+^{12}\text{C}$  resonances have also been studied recently within the molecular model framework by Schmidt and Scheid [82]. However, in this case the spin alignment observed in the experimental data [76] has still to be understood within the molecular picture.

#### D. Alternative theoretical calculations of the $^{28}\text{Si}+^{28}\text{Si}$ scattering

The structural configuration of the molecular resonance states populated in  $^{28}\text{Si}+^{28}\text{Si}$  scattering has also been studied within an orbiting cluster model approach [84]. A generalized moment of inertia expression that applies to the  $^{56}\text{Ni}$  dinuclear configuration, rather than a mononuclear one is based on the two-center shell model [2] (TCSM). However, the oblate nature of the  $^{28}\text{Si}$  nucleus has yet to be included properly in this model and, thus, more refined TCSM calculations are highly desirable. The generator coordinate and resonating group methods have been applied for the  $^{28}\text{Si}+^{28}\text{Si}$  reaction with the double-resonance model by Langanke *et al.* [85] to explain, with some success, both the gross structure [7] and intermediate structure [8] present in the experimental excitation functions. Similarly, Thiel *et al.* [86] have used the nuclear molecular concept to analyze the  $^{28}\text{Si}+^{28}\text{Si}$  cross sections on the basis of coupled-channel calculations. They have shown [86] for the first time that the theoretical concepts of a double-resonance model developed and applied successfully [2] for lighter systems can be extended to heavier ones. The broad structures in the excitation functions [7] of the  $80^\circ$  and  $90^\circ$  differential cross sections, measured with a 1 MeV step size, for the elastic scattering and single excitation to the  $2^+$  state in  $^{28}\text{Si}$  are well reproduced. However, the intermediate-width structures evident in the 100-keV step size excitation function [9] are not reproduced. The angular distributions for the elastic, single and

mutual inelastic channels have been fairly well reproduced at  $E_{\text{lab}}=120$  MeV by these coupled channel calculations (see Ref. [2], and references therein) with a potential assuming barriers located at quite large relative distances (8 fm). However, the large oscillations calculated forward of  $60^\circ$  are not present in the data [8]. The large value of the relative distance corresponds to a radius where the charge density of  $^{28}\text{Si}$  is reduced to 5% of its maximum value. It reflects the softness of the  $^{28}\text{Si}$  nuclei when they touch each other. Another attempt to account for the low resolution data was made using projection methods within the framework of the doorway model [73]. Similar coupled channel calculations are highly desirable for the  $J^\pi=38^+$  resonance at  $E_{\text{lab}}=111.6$  MeV. Many-particle many-hole calculations [40] using the Hartree-Fock approach have been carried out for  $^{56}\text{Ni}$ , and a highly deformed  $16p-16h$  band has been found to reproduce the sequence of resonances observed for  $^{28}\text{Si}+^{28}\text{Si}$  between the resonant energies with  $J=36\hbar$  and  $J=40\hbar$ , including the  $38^+$  resonance. It is thus reasonable to consider associating these molecular resonances with the shape isomers calculated in the Hartree-Fock formalism [40].

## VI. SUMMARY AND CONCLUSIONS

The  $J=38\hbar$  resonance observed in  $^{28}\text{Si}+^{28}\text{Si}$  data at  $E_{\text{lab}}=111.6$  MeV has been studied by both fragment-fragment and fragment-fragment- $\gamma$  coincidence measurements. From the analysis of the particle angular distributions of the mass-symmetric  $^{28}\text{Si}+^{28}\text{Si}$  exit channel, it can be concluded that, at the resonance energy, the spin vectors of the  $^{28}\text{Si}$  fragments do not couple with the orbital angular momentum, leading to  $m=0$ . This result was not anticipated and is sharp contrast with similar measurements for the  $^{12}\text{C}+^{12}\text{C}$  and  $^{24}\text{Mg}+^{24}\text{Mg}$  systems. The fragment-fragment- $\gamma$  coincidence data demonstrate that for the  $^{28}\text{Si}$  fragments, the mutually excited states are the most strongly populated. The population of states of the  $K^\pi=3_1^-$  band appears to be a rather strong indication of an *oblate* deformed shape for the fragments.

The general overall good agreement between data and a transition-state model calculation at higher excitation energies suggests that statistical fission decay is important in both the  $^{28}\text{Si}+^{28}\text{Si}$  and  $^{32}\text{S}+^{24}\text{Mg}$  exit channels, while the resonance behavior appears to involve preferentially the low-lying states of the mass-symmetric channel. The TSM calculations describe both the structures observed at high excitation energy in the fission  $Q$ -value spectra and the population pattern of states in the  $^{28}\text{Si}$  fission fragments. Although the lack of off-resonance data may limit some of the conclusions that can be drawn from this work, the observations do favor the calculations of the molecular model of Uegaki and Abe [44], which predict a vanishing spin alignment for the  $^{28}\text{Si}+^{28}\text{Si}$  system at the resonance energy. The calculations are also consistent with the experimentally observed alignment in the  $^{24}\text{Mg}+^{24}\text{Mg}$  collisions. Overall, the results of this paper provide further support for recent theoretical investigations that view the resonances in terms of shape-isomeric states stabilized in hyperdeformed secondary minima. However, a more global understanding will surely

require a more fundamental synthesis of the theories which describe reaction mechanisms with those describing nuclear structure at high excitation energy and angular momentum.

In conclusion, this experimental study develops new evidence about the precise mechanism(s) involved in the formation of molecular resonances. The exclusive experiments that are now becoming feasible with large  $\gamma$ -ray facilities, such as EUROBALL and GAMMASPHERE, will allow precise determinations of the spins and the molecular structures of the  $^{24}\text{Mg}+^{24}\text{Mg}$  and  $^{28}\text{Si}+^{28}\text{Si}$  resonances. Such knowledge can be expected to more generally enhance our understanding of highly deformed nuclear systems.

#### ACKNOWLEDGMENTS

This paper is based upon the Ph.D. thesis of R. Nouicer, Université Louis Pasteur de Strasbourg, 1997. The coopera-

tion and assistance of the staff of the VIVITRON is gratefully acknowledged for providing us with good quality, stable  $^{28}\text{Si}$  beams. The authors wish to thank the EUROGAM staff of IReS (and, more particularly, J. Devin, D. Prévost, and C. Ring) and J.P. Vivien for the reliable functioning of the multidetector array, and for precious help during the experiment. EUROGAM is jointly funded by IN2P3 (France) and EPSRC (U.K.). Two of us (C.B. and R.N.) would like also to acknowledge Y. Abe and E. Uegaki for their stimulating theoretical help in the initial stages of this work and helpful discussions. R.V.F. Janssens and W. von Oertzen are thanked for a careful reading of the manuscript. This work was sponsored by the French CNRS/IN2P3, and by CNRS/NSF and CNRS/CNPq collaboration programs, and also in part by the U.S. DOE under Grant No. DE-FG03-96-ER40981.

- 
- [1] K. Erb and D. A. Bromley, *Treatise on Heavy-Ion Science*, edited by D. A. Bromley (Plenum, New York, 1985), Vol. 3, p. 201, and references therein.
- [2] W. Greiner, J. Y. Park, and W. Scheid, *Nuclear Molecules* (World Scientific, Singapore, 1995), and references therein.
- [3] R. R. Betts and A. H. Wuosmaa, *Rep. Prog. Phys.* **60**, 819 (1997), and references therein.
- [4] D. A. Bromley, J. A. Kuehner, and E. Almqvist, *Phys. Rev. Lett.* **4**, 365 (1960); **4**, 515 (1960).
- [5] T. M. Cormier, *Annu. Rev. Nucl. Part. Sci.* **32**, 271 (1982), and references therein.
- [6] R. R. Betts, *Nucl. Phys.* **A447**, 257c (1985).
- [7] R. R. Betts, S. B. DiCenzo, and J. F. Petersen, *Phys. Rev. Lett.* **43**, 253 (1979).
- [8] R. R. Betts, S. B. DiCenzo, and J. F. Petersen, *Phys. Lett.* **100B**, 117 (1981).
- [9] R. R. Betts, B. B. Back, and B. G. Glagola, *Phys. Rev. Lett.* **47**, 23 (1981).
- [10] R. R. Betts and S. Saini, *Phys. Scr.* **T5**, 204 (1983).
- [11] R. R. Betts, *Proceedings of the International Conference on Nuclear Physics with Heavy Ions*, Stony Brook, 1983, edited by P. Braun-Munzinger (Harwood, New York, 1984).
- [12] S. Saini and R. R. Betts, *Phys. Rev. C* **29**, 1769 (1984).
- [13] R. W. Zurmühle, P. Kutt, R. R. Betts, S. Saini, F. Haas, and O. Hansen, *Phys. Lett.* **129B**, 384 (1983).
- [14] S. Saini, R. R. Betts, R. W. Zurmühle, P. H. Kutt, and B. K. Dichter, *Phys. Lett.* **185B**, 316 (1987).
- [15] A. H. Wuosmaa, R. W. Zurmühle, P. H. Kutt, S. F. Pate, S. Saini, M. L. Halbert, and D. C. Hensley, *Phys. Rev. Lett.* **58**, 1312 (1987).
- [16] A. Mattis, W. Dünnweber, W. Trombik, A. Glaesner, W. Hering, D. Konnerth, and R. Ritzka, *Phys. Lett. B* **191**, 328 (1987).
- [17] A. H. Wuosmaa, R. W. Zurmühle, P. H. Kutt, S. F. Pate, S. Saini, M. L. Halbert, and D. C. Hensley, *Phys. Rev. C* **41**, 2666 (1990).
- [18] A. H. Wuosmaa, S. Saini, P. H. Kutt, S. F. Pate, R. W. Zurmühle, and R. R. Betts, *Phys. Rev. C* **36**, 1011 (1987).
- [19] A. H. Wuosmaa, S. F. Pate, and R. W. Zurmühle, *Phys. Rev. C* **40**, 173 (1989).
- [20] P. H. Kutt, S. F. Pate, A. H. Wuosmaa, R. W. Zurmühle, O. Hansen, R. R. Betts, and S. Saini, *Phys. Lett.* **155B**, 27 (1985).
- [21] C. Beck, Y. Abe, N. Aissaoui, B. Djerrou, and F. Haas, *Phys. Rev. C* **49**, 2618 (1994).
- [22] C. Beck, Y. Abe, N. Aissaoui, B. Djerrou, and F. Haas, *Nucl. Phys.* **A583**, 269 (1995).
- [23] C. Beck and A. Szanto de Toledo, *Phys. Rev. C* **53**, 1989 (1996).
- [24] S. J. Sanders, A. Szanto de Toledo, and C. Beck, *Phys. Rep.* **311**, 487 (1999), and references therein.
- [25] S. J. Sanders, R. R. Betts, I. Ahmad, K. T. Lesko, S. Saini, B. D. Wilkins, F. Videbaek, and B. K. Dichter, *Phys. Rev. C* **34**, 1746 (1986).
- [26] B. K. Dichter, P. D. Parker, S. J. Sanders, R. R. Betts, and S. Saini, *Phys. Rev. C* **35**, 1304 (1987).
- [27] C. Beck *et al.*, *Phys. Rev. C* **39**, 2202 (1989), and references therein.
- [28] S. J. Sanders *et al.*, *Phys. Rev. Lett.* **59**, 2856 (1987).
- [29] S. J. Sanders, D. G. Kovar, B. B. Back, C. Beck, D. J. Henderson, R. V. F. Janssens, T.-F. Wang, and B. D. Wilkins, *Phys. Rev. C* **40**, 2091 (1989).
- [30] S. J. Sanders *et al.*, *Phys. Rev. C* **41**, R1901 (1990).
- [31] S. J. Sanders *et al.*, *Phys. Rev. C* **49**, 1016 (1994).
- [32] S. Thummerer *et al.*, *Phys. Scr.* **T88**, 114 (2000); S. Thummerer, W. von Oertzen, B. Gebauer, D. R. Napoli, S. M. Lenzi, A. Gadea, C. Beck, and M. Rousseau, *J. Phys. G* (to be published).
- [33] S. J. Sanders, *Phys. Rev. C* **44**, 2676 (1991).
- [34] T. Matsuse, C. Beck, R. Nouicer, and D. Mahboub, *Phys. Rev. C* **55**, 1380 (1997).
- [35] C. Beck, *Acta Phys. Pol. B* **30**, 1527 (1999).
- [36] K. A. Farrar *et al.*, *Phys. Rev. C* **54**, 1249 (1996).
- [37] T. Bengtsson, M. E. Faber, G. Leander, P. Moller, M. Ploszajczak, I. Ragnarsson, and S. Aberg, *Phys. Scr.* **24**, 200 (1981).
- [38] T. Bengtsson, M. Faber, M. Ploszajczak, I. Ragnarsson, and S. Aberg, Report No. MPh-84/01, Lund Institute of Technology, Sweden, 1984 (unpublished).

- [39] S. Aberg, in *Proceedings of the Workshop on the Interface Between Nuclear Structure and Heavy-Ion Reaction Dynamics*, University of Notre Dame, edited by R. R. Betts and J. J. Kolata (IOP, Bristol, 1991), p. 143.
- [40] D. C. Zheng, L. Zamick, and D. Berdichevsky, *Phys. Rev. C* **42**, 1004 (1990).
- [41] J. Zhang, A. C. Merchant, and W. D. M. Rae, *Phys. Rev. C* **49**, 562 (1994).
- [42] E. Uegaki and Y. Abe, *Phys. Lett. B* **231**, 28 (1989).
- [43] E. Uegaki and Y. Abe, *Prog. Theor. Phys.* **90**, 615 (1993).
- [44] E. Uegaki and Y. Abe, *Phys. Lett. B* **340**, 143 (1994).
- [45] E. Uegaki, *Suppl. Prog. Theor. Phys.* **132**, 135 (1998).
- [46] E. Uegaki and Y. Abe, in *Proceedings of the 7th International Conference on Clustering Aspects of Nuclear Structure and Dynamics*, edited by M. Korolija, Z. Basrak, and R. Caplar (World Scientific, Singapore, 2000), p. 160.
- [47] R. Nouicer *et al.*, *Phys. Rev. C* **60**, 041303(R) (1999).
- [48] S. Yu Kun, B. A. Robson, and A. V. Vagov, *Phys. Rev. Lett.* **83**, 504 (1999).
- [49] P. J. Nolan, F. A. Beck, and D. B. Fossan, *Annu. Rev. Nucl. Sci.* **44**, 561 (1994).
- [50] R. R. Betts, H.-G. Clerc, B. B. Back, I. Ahmad, K. L. Wolf, and B. G. Glagola, *Phys. Rev. Lett.* **46**, 313 (1981).
- [51] R. M. Freeman, C. Beck, F. Haas, A. Morsad, and N. Cindro, *Phys. Rev. C* **33**, 1275 (1986).
- [52] R. Nouicer, Ph.D. thesis, University of Strasbourg, 1997, Internal Report No. IReS-97-35 (unpublished).
- [53] R. Nouicer *et al.*, *Ric. Sci. Educ. Permanente Suppl.* **112**, 473 (1998).
- [54] C. W. Beausang *et al.*, *Nucl. Instrum. Methods Phys. Res. A* **313**, 37 (1992).
- [55] G. Duchêne *et al.*, *Nucl. Instrum. Methods Phys. Res. A* **432**, 90 (1999).
- [56] R. Nouicer *et al.*, *Heavy Ion Physics*, edited by Yu. Ts. Oganessian and R. Kalpakchieva (World Scientific, Singapore, 1998), p. 538.
- [57] S. B. DiCenzo, J. F. Petersen, and R. R. Betts, *Phys. Rev. C* **23**, 2561 (1981); S. B. DiCenzo, Ph.D. thesis, Yale University, 1980.
- [58] R. M. Freeman, F. Haas, M.-P. Nicoli, A. Morsad, and Z. Basrak, *Eur. Phys. J. A* **4**, 239 (1999).
- [59] M. F. Vineyard *et al.*, *Phys. Rev. C* **41**, 1005 (1990), and references therein.
- [60] F. Glatz, P. Betz, J. Siefert, P. Heidinger, and H. Röpke, *Phys. Rev. Lett.* **46**, 1559 (1981).
- [61] F. Glatz *et al.*, *Z. Phys. A* **303**, 239 (1981).
- [62] F. Glatz *et al.*, *Z. Phys. A* **324**, 173 (1986).
- [63] P. M. Endt, *Nucl. Phys.* **A521**, 1 (1990).
- [64] J. Brenneisen *et al.*, *Z. Phys. A* **352**, 149 (1995); **352**, 157 (1995); **352**, 403 (1995).
- [65] J. Zhang and W. D. M. Rae, *Nucl. Phys.* **A564**, 252 (1993); J. Zhang, W. D. M. Rae, and A. C. Merchant, **A575**, 61 (1994).
- [66] J. Brenneisen *et al.*, *Z. Phys. A* **357**, 157 (1997).
- [67] A. Kangasmäki, P. Tikkanen, J. Keikonen, W. E. Ormand, S. Raman, Zs. Fülöp, A. Z. Kiss, and E. Somorjai, *Phys. Rev. C* **58**, 699 (1998), and references therein.
- [68] J. Brenneisen, B. Erhardt, F. Glatz, Th. Kern, R. Ott, H. Röpke, J. Schmalzlin, P. Siedle, and B. H. Wildenthal, *Z. Phys. A* **357**, 377 (1997).
- [69] J. Cseh, G. Lévai, A. Ventura, and I. Zuffi, *Phys. Rev. C* **58**, 2144 (1998).
- [70] H. Molière, J. Dobaczewski, and J. Dudek, *Phys. Rev. C* **61**, 044304 (2000).
- [71] M. Yamagami and K. Matsuyanagi, *Nucl. Phys.* **A672**, 123 (2000).
- [72] O. Tanimura and T. Tazawa, *Phys. Lett.* **78B**, 1 (1978).
- [73] S. A. Khan and W. P. Beres, *Phys. Rev. C* **32**, 871 (1985).
- [74] M. Carchidi and B. H. Wildenthal, *Phys. Rev. C* **37**, 1681 (1988).
- [75] W. Dünneweber, A. Glaesner, W. Hering, D. Konnerth, R. Ritzka, W. Trombik, J. Czakanski, and W. Zipper, *Phys. Rev. Lett.* **61**, 927 (1988).
- [76] D. Konnerth, W. Trombik, K. G. Bernhardt, K. A. Eberhard, R. Singh, A. Strzalkowski, and W. Trautmann, *Phys. Rev. Lett.* **55**, 588 (1985).
- [77] Y. Kondo, Y. Abe, and T. Matsuse, *Phys. Rev. C* **19**, 1356 (1979).
- [78] R. Maass and W. Scheid, *Phys. Lett. B* **202**, 26 (1988).
- [79] R. Maass and W. Scheid, *J. Phys. G* **16**, 1359 (1990).
- [80] R. Maass and W. Scheid, *J. Phys. G* **18**, 707 (1992).
- [81] B. B. Back, *Phys. Rev. C* **31**, 2104 (1985).
- [82] J. Schmidt and W. Scheid, *Phys. Rev. C* **53**, 322 (1996).
- [83] P. O. Hess, W. Greiner, and W. T. Pinkston, *Phys. Rev. Lett.* **53**, 1535 (1984).
- [84] H. S. Khosla, S. S. Malik, and R. K. Gupta, *Nucl. Phys.* **A513**, 115 (1990).
- [85] K. Langanke, R. Stedenman, and A. Weiguny, *Phys. Lett.* **112B**, 116 (1982).
- [86] A. Thiel, W. Greiner, and W. Scheid, *Phys. Rev. C* **29**, 864 (1984).